Tailoring Porosity and Rotational Dynamics in a Series of Octacarboxylate Metal-Organic Frameworks

Florian Moreau,[a] Daniil I. Kolokolov,[b,c] Alexander G. Stepanov,[b,c] Timothy L. Easun,[d] Anne Dailly,[e] William Lewis,[f] Alexander J. Blake,[f] Harriott Nowell,[g] Matthew J. Lennox,[f] Elena Besley,[f] Sihai Yang[a]* and Martin Schröder[a,h]*

[a] School of Chemistry, University of Manchester, Oxford Road, Manchester M13 9PL, UK.
[b] Boreskov Institute of Catalysis, Siberian Branch of Russian Academy of Sciences, Prospekt Akademika Lavrentieva 5, Novosibirsk 630090, Russia.
[c] Novosibirsk State University, Pirogova Street 2, Novosibirsk 630090, Russia.
[d] School of Chemistry, Cardiff University, Main Building, Park Place, Cardiff CF10 3AT, UK.
[e] General Motors Global Research and Development Center, Warren, MI, USA
[f] School of Chemistry, University of Nottingham, University Park, Nottingham NG7 2RD, UK.
[g] Diamond Light Source, Harwell Science Campus, Oxon, OX11 0DE, UK.
[h] Nikolaev Institute of Inorganic Chemistry, Siberian Branch of the Russian Academy of Sciences, 3 Acad. Lavrentiev Ave., Novosibirsk, 630090, Russia.

Email: Sihai.Yang@manchester.ac.uk; M.Schroder@manchester.ac.uk

Keywords: metal organic framework, crystal engineering, methane, ^{2}H NMR, molecular dynamics

Precise control of porosity and pore decoration in metal organic framework (MOFs) materials are of critical importance to their function. Here we report the first example of modulation of porosity for a series of isoreticular MOFs denoted MFM-180 to MFM-185 derived from octacarboxylate linkers *via* a strategy of selective elongation of metal organic cages. The highly connected linkers assemble with Cu(II) to give non-interpenetrated, porous tbo or 3,3,4-c nets in which octahedral cages are connected to generate two further cuboctahedral cages of fixed diameter. The larger pores are defined by the systematic and controlled elongation of the ligand linkers that range from a simple ethylenyl moiety in MFM-180 to a five-fused heteropolyaromatic core as in MFM-185. Activated MFM-185a shows a record high BET surface area of 4734 $m^2 g^{-1}$ for a material derived from octacarboxylate linkers. These MOFs show remarkable CH_4 and CO_2 adsorption properties, notably with simultaneously high gravimetric and deliverable volumetric CH_4 capacities of 0.24 g g^{-1} and 163 v/v (298 K, 5-65 bar) recorded for MFM-185a. The dynamics of molecular rotors in deuterated MFM-180a-d_{16} and MFM-181a-d_{16} have been investigated by variable-temperature ^2H solid state NMR spectroscopy to reveal the re-orientation mechanisms within these materials. Analysis of the flipping modes of the mobile phenyl groups in the linkers, their rotational rates and transition temperatures, paves the way to controlling and understanding the role of molecular rotors within porous MOF materials.

Metal-organic frameworks (MOFs) are an emerging class of porous, multifunctional materials showing great potential in a wide range of applications.[1–7] Given their metal-organic hybrid nature, MOFs have an exceptionally high degree of structural diversity and tailorability.[8] Thus, not only is the on-demand design of materials that incorporate pores of precise shape and dimension achievable, but also the inner surface of these materials becomes a platform for incorporation of designed functionality for target applications.[9,10] Within the field of gas storage, there is a strong correlation between the material porosity and the maximum adsorption capacity. A common strategy to increase porosity in MOFs consists of targeting a framework topology and systematically elongating the linkers to generate additional pore space. This approach has shown success in a number of MOF systems,[1,2,6,11] but is not without its drawbacks. For example, increases in porosity typically correlate to increases in pore diameters, which can be detrimental to the strength of host-guest interactions at low surface coverage.[11] Also, often, simple ligand-elongation will ultimately lead to framework interpenetration with reduced porosity and/or stability.[12-14] Powerful drivers therefore exist to find the ideal compromise between high porosity and strong host-guest interactions over a wide range of pressures.

The use of rigid, highly-connected linkers (*e.g.* with 6 to 8 coordinating functions) affords potentially a more robust and stable platform for the development of isoreticular porous materials. This strategy has been widely implemented for $[Cu_2(O_2CR)_4]$ paddlewheel systems with hexacarboxylate linkers of C_3-symmetry to generate a family of ***rht***-type MOFs with high and predictable porosity.[15-17] In contrast, effective modulation of porosity for isoreticular MOFs based upon 8-connected linkers[18-26] has not been achieved to date, and thus represents a significant synthetic challenge. We report herein the first example of modulation of porosity in a series of isoreticular octacarboxylate MOFs. By varying the length and nature of the heteropolyaromatic cores of the linkers, we have selectively extended the length of metal-organic cages in a single direction on going from MFM-180 to MFM-185 and due to the high connectivity effectively avoiding framework interpenetration as well. We also report the temperature-dependent ^{2}H NMR studies of selectively deuterated MFM-180-d_{16} and MFM-181-d_{16} to define the rotational and flipping modes of the phenyl groups within these structures in the solid state. The dynamics of molecular rotors (*e.g.*, phenyl rings) within MOF materials is a key property to their functionalisation as they form part of the internal pore surface and are thus highly sensitive to the presence of guest molecules.[27-31] In this regard, the series of MOFs herein offer a unique platform to probe the influence of altering the ligand structure on the molecular dynamics and rotational freedom within the resultant framework.

RESULTS AND DISCUSSION

Design and synthesis of octa-connected ligands and isoreticular MOFs. The series of octa-connected linkers, ranging from 19 to 30 Å in length, are shown in Figure 1 and their syntheses are described in SI. H_8L^0, H_8L^3 and H_8L^5 were synthesized by direct Suzuki-Miyaura coupling of

diethylisophthalate-5-boronic acid with the corresponding tetrahalides: 1,1,2,2-tetrakis(4-bromophenyl)ethane, 2,3,7,8-tetrakis(4-bromophenyl)pyrazino[2,3-*g*]quinoxaline, and 2,3,9,10-tetrakis(4-bromophenyl)-[1,4]dioxino[2,3-*g*:5,6-*g*']diquinoxaline for H_8L^0, H_8L^3, and H_8L^5, respectively. In the case of H_8L^1 and H_8L^2, we employed a different strategy where the extended 3',5'-bis(ethoxycarbonyl)biphenyl-4-ylboronic acid was coupled with 1,2,4,5-tetrabromobenzene and 2,3,6,7-tetraiodonaphthalene, respectively. Attempts to prepare H_8L^4 from naphthalene-2,3,6,7-tetraamine failed, and therefore the target MOF MFM-184 was analysed *in silico* based upon the isoreticular nature of the series of MOFs in this study. Solvothermal reactions of H_8L^0, H_8L^1, H_8L^2 or H_8L^3 with $CuCl_2$ in a mixture of DEF/ethanol/0.1M aqueous HCl (2/2/1, v/v/v) at 80 °C for 16 h afforded the solvated materials $[Cu_4(L^n)(H_2O)_4]_\infty \cdot$solv or MFM-18n (n = 0, 1, 2, 3). Due to the insolubility of H_8L^5 in the above solvent mixture, the synthesis of MFM-185 was conducted in a mixture of DMF/DMSO/2M aqueous HCl (40/20/1, v/v/v) with $Cu(NO_3)_2.2.5H_2O$ for 4 days. The "indirect" synthesis of $[Cu_4(L^0)(H_2O)_4]_\infty$ has been reported previously *via* transmetallation of the iso-structural $[Zn_4(L^1)(H_2O)_4]_\infty$ complex, in which Zn(II) ions are gradually replaced by Cu(II) ions.[24]

Analysis of the crystal structures. The X-ray single crystal structures of MFM-180, -181, -182, -183 and -185 confirm the formation of square planar $[Cu_2(O_2CR)_4]$ nodes bridged by the octacarboxyate linkers to afford 3D open structures. MFM-180 crystallizes in the tetragonal space group $I\bar{4}2m$ with a = 18.6924(2) Å and c = 35.9196(4) Å. The octacarboxylate linker $[L^0]^{8-}$ is comprised of a central tetraphenylethylene core bearing four isophthalate moieties in 4,4',4'',4''' positions and acts as a 4-connected node (Figure 1). Each isophthalate arm is orthogonal to the main plane of the molecule and acts as a 3-connected node. Each linker connects to eight $[Cu_2(O_2CR)_4]$ paddlewheels, and each paddlewheel connects to four independent linkers. As a result, the MFM-180 framework can be regarded as a 3,3,4-c ***tbo*** net (Figure S1) of stoichiometry $(3\text{-c})_4(4\text{-c})_3$ with the corresponding point symbol of $\{6^2.8^2.10^2\}_3\{6^3\}_4$.[32] The metal-ligand linkage affords three types of metal-organic cages (A, B, and C with a ratio of 2:1:1), the smallest of which is an elongated octahedral cage A comprising two ligands and four $[Cu_2(O_2CR)_4]$ paddlewheels (Figure 2). The $[Cu_2(O_2CR)_4]$ moieties occupy the four equatorial vertices while two ethylene groups from the ligands occupy the apical vertices. The overall structure results from the corner-sharing assembly of these octahedral cages A *via* ethylene groups along the *c* axis and $[Cu_2(O_2CR)_4]$ paddlewheels along the *a*/*b* axis. This arrangement generates two types of elongated cuboctahedra cages, each one comprising four ligands and eight $[Cu_2(O_2CR)_4]$ paddlewheels. The largest spheres that can fit within these cages taking into account the van der Waals radii of surface atoms have diameters of 3.0, 13.2 Å and 10.4 Å for cages A, B and C, respectively.

In previously reported examples of octacarboxylate MOFs with **tbo** or **scu** nets,[18-26] the linkers presented a central four-connected node with increasing distances between the central node and four isophthalate moieties. Although this strategy produced isoreticular MOFs, no increase of porosity was

observed, presumably because of framework flexibility and/or formation of highly strained structures. As an alternative approach to simply extending the linker length along all directions, we sought to target the extension of specific dimensions and lengths to better control the porosity of resultant MOFs. The distance l_1 (Figure 1) is crucial for the formation of the octahedral cages A because it codes for the overall structural assembly. In contrast, the distance l_2 defines the length of cages B and C, and thus we sought to design linkers in which l_1 remains constant but l_2 is augmented. For this purpose, we replaced the four-connected ethylene bond from the ligand H_8L^0 with a series of extended aromatic cores. The targeted isoreticular MOFs (except for MFM-184) were obtained as single crystals and their structures confirmed by single crystal diffraction.

Replacement of the ethylenyl core in MFM-180 with a benzene ring affords MFM-181 which crystallizes in a different tetragonal space group *I*4/*mmm*. The change in space group is due to the presence of structural disorder in MFM-181, in which the free rotating phenyl rings are disordered over two positions. Nonetheless, MFM-181 exhibits the same ***tbo*** topology as MFM-180 (Figure S1) when the phenyl core is considered as a four-connected node. The octahedral cage A in MFM-181 is retained as expected. Cages B and C in MFM-181 are elongated along the *c* axis by 2.65 Å in comparison with MFM-180. The length of linkers $[L^2]^{8-}$, $[L^3]^{8-}$ and $[L^5]^{8-}$ is further increased by incorporating central cores of naphthalene, three- and five-fused heteroacenes, respectively. The corresponding MOFs, MFM-182, MFM-183 and MFM-185, all crystallize in the space group *I*4/*mmm* with the same structure. Given the extension of the polyaromatic cores of $[L^2]^{8-}$, $[L^3]^{8-}$ and $[L^5]^{8-}$, the most accurate topological description of the underlying nets of MFM-182, MFM-183 and MFM-185 reflects a process called "decoration" in which a net vertex is replaced by a group of vertices. Thus, MFM-182, MFM-183 and MFM-185 present the same previously unreported 3,3,4-c net with point symbol: $\{6.10^2\}\{6^2.8^2.10^2\}\{6^3\}_2$ which is derived from the **tbo** net by decoration of half of its 4-c vertices by a pair of 3-c vertices (Figure S1). The calculated accessible voids (PLATON) are 71.5%, 71.2%, 73.3 %, 75.4 % and 76.7 % for MFM-180, MFM-181, MFM-182, MFM-183 and MFM-185, respectively.

Modulation of porosity and gas adsorption property. Activated MFM-180a and MFM-181a were obtained by heating the methanol-exchanged samples at 100 °C under dynamic vacuum for 16 h. Supercritical CO_2 drying was employed to prepare activated MFM-183a and -185a to maximise the retention of their pore structure. MFM-180a, -181a, -183a, and 185a show BET surface areas of 2610, 3100, 4130 and 4730 $m^2 g^{-1}$, respectively, as determined from N_2 adsorption at 77 K. The BET surface areas for MFM-182a and MFM-184a are predicted by GCMC to be 3557 and 4289 $m^2 g^{-1}$, respectively, since difficulties in preparing pure bulk materials precluded experimental measurement of their isotherms (see SI). Analysis of the N_2 isotherms using a nonlocal density functional theory (NLDFT) model revealed the pore size distribution centered around 13.3, 13.7, 14.3, and 16.3 Å for MFM-180a, -181a, -183a and 185a, respectively. Additionally, total pore volumes of 1.00, 1.36, 1.45

and 1.65 cm^3 g^{-1} were obtained from the N_2 isotherms, and compare favourably with that calculated based upon single crystal structures (1.09, 1.19, 1.40 and 1.59 cm^3 g^{-1} for MFM-180a, -181a, -183a and -185a). The results confirm the complete activation of these MOFs and are consistent with the increasing pore dimensions across the series. To the best of our knowledge, MFM-185a possesses the highest BET surface area and pore volume among octacarboxylate MOFs.

The CH_4 adsorption capacities of MFM-181a, -183a, and 185a are among the highest reported values for the best behaving MOFs at 35 bar, 298 K (Figure 3, Table S6). Interestingly, the intrinsic trade-off between gravimetric and volumetric capacities is minimised in this series of MOFs owing to the high framework connectivity and thus relatively high crystal density in comparison to other highly porous MOFs.[17] For example, both gravimetric and volumetric CH_4 adsorption capacities of MFM-181a, -183a, and 185a are higher than those reported for the more porous octacarboxylate MOF PCN-80a (17.7 wt %, 142 v/v)[1] under same conditions. CH_4 adsorption in MFM-181a is saturated at 55 bar, whereas MFM-183a and MFM-185a can accommodate more CH_4 molecules at higher pressures owing to their extended pore space. At 65 bar, the total gravimetric uptake of MFM-185a is sufficiently high (29.0 wt %) to compensate for its low crystal density and hence it displays the highest volumetric CH_4 uptake (198 v/v) of the series. Since MFM-181a, 183a and 185a have almost identical CH_4 uptakes at 298 K and 5 bar, the desirable improvement of the materials porosity through elongation of the metal-organic cages affords a predictable increase in both gravimetric and volumetric "working capacities" (defined as the difference in total uptake between 65 and 5 bar). For example, MFM-185 shows the highest deliverable CH_4 capacity in both gravimetric and volumetric terms among all octacarboxylate MOFs (Table S6).

The CO_2 adsorption isotherms were recorded at 298 K up to 20 bar for MFM-180a, -181a, -183a, and 185a (Figure 3). The isosteric heats of CO_2 adsorption were estimated to be around 23 kJ mol^{-1} for all MOFs (Table S7). At low pressure (1 bar), both gravimetric and volumetric CO_2 uptakes are higher for the less porous frameworks, ranging from 13.0 wt % (32.2 v/v) for MFM-185a to 15.0 wt % (54.9 v/v) for MFM-180a, which suggests that a high density of open metal sites is crucial to maximise the low pressure CO_2/framework interactions. For pressures higher than 10 bar, the larger pore volume of MFM-185a allows it to reach the highest gravimetric uptake (107.3 wt % at 20 bar) of the series whereas MFM-181a shows the highest volumetric CO_2 uptake (292.4 v/v at 20 bar) due to its combination of large surface area and moderately low density. These uptakes compare favourably with other octacarboxylate MOFs presenting higher (PCN-80a[25]: 72.8 wt % at 20 bar, 293 K) or similar (MFM-140[18]: 91.2 wt % at 20 bar, 298 K) porosities.

^{2}H NMR spectroscopic studies on the dynamics of molecular rotors. Solid-state ^{2}H NMR spectroscopy was used to investigate the molecular dynamics of the phenyl rings in this series of MOFs. MFM-180a and MFM-181a were partially deuterated on the mobile aromatic rings in the ligands to give MFM-180a-d_{16} and MFM-181a-d_{16} (see SI). Variable temperature ^{2}H NMR

spectroscopic studies on MFM-180a-d_{16} and MFM-181a-d_{16} (Figure 4 and SI) show that the mobility of the phenyl groups for both materials evolves with temperature starting from a Pake-powder pattern with quadrupolar coupling parameters (Q_0 = 176 kHz, η = 0) typical for static phenyl groups at low temperature. The evolution of the line shape with rising temperature depicts a re-orientation mechanism similar for both MOFs with three regimes: (i) from low temperatures (123 K) up to T_1, the line shape evolves to a typical two-site exchange pattern;[33] (ii) above T_1, the line shape remains stable up to T_2, and (iii) above T_2 it evolves to yield a narrowed uniaxial Pake-pattern (Q_1 = 21 kHz ~ Q_0/8, η = 0), indicating that the phenyl fragments rotate homogeneously around the C_2 axis. Although the uniaxial ligand rotation in MOFs has been reported,[35] the complex hierarchical dynamic behavior in MFM-180a-d_{16} and MFM-181a-d_{16} has not been observed previously.

The striking difference between MFM-180a-d_{16} and MFM-181a-d_{16} lies in the temperatures of transition from one motional mode to another, from two-site flipping to continuous rotation. For MFM-180a-d_{16}, T_1 is ~ 310 K and T_2 is ~ 330 K, while in MFM-181a-d_{16}, T_1 is ~ 200 K, and T_2 remains at 330 K. This result indicates that changes in the ligand core affect only one of the two rotational modes, with the flipping mode that evolves below T_1 being notably faster for MFM-181a-d_{16}. Significantly, this is the first time such observation has been made in MOFs and opens up the possibility to design the rotational potential of mobile fragments within such porous materials.

The line shape interpretation is based on the following general considerations. The position of mobile phenyl groups in the framework leaves freedom only for rotation or flipping about the C_2 axis and the angle between the rotation axis and the C-D bond is naturally fixed to be θ_{ph} = 60° (Figure 5a). Therefore, the simplest model that can describe the line shape evolution is the four-site jump-exchange rotation for the torsional angle φ covering the whole 360° range (Figure 5b). In such a scheme each of the two C-D bonds flips between two sites (φ_1 <> φ_2 and φ_3 <> φ_4) displaced by a jump angle $\Delta\varphi_1$. When the temperature conditions are met and the phenyl ring is able to overcome the second rotational barrier between the sites φ_1 <> φ_3 and φ_2 <> φ_4 each C-D bonds begins to perform the full 360° rotation. In each pair only the highest barrier is relevant, and thus the motion can be described by the two independent rate constants k_1 and k_2. This model is evidenced by its excellent fit with the experimental data for both samples (Figure 4). The two-site exchange motion governing the line shape below T_2 allows the determination of the exact position for C-D bond sites. For MFM-180a-d_{16}, the jump angle $\Delta\varphi_1^{I}$ = 71°, while for MFM-181a-d_{16}, $\Delta\varphi_1^{II}$ = 68°. The second jump angle can then be readily computed as $\Delta\varphi_2^{i}$ = 180° - $\Delta\varphi_1^{i}$. This shows that the equilibrium positions are displaced compared to an ideal C_4 symmetry. The line shape evolution above T_2 fully supports the four sites exchange model and excludes any other interpretation of the observed spectra. Most intriguing are the potential barriers and collision factors involved. In all cases, the rotation rates follow the standard Arrhenius law (Figure 6). For k_1 in MFM-180a-d_{16} the parameters are E_1 = 26 kJ mol^{-1} and k_{10} = 1.6x10^{11}, and for MFM-181a-d_{16} E_1 = 20 kJ mol^{-1} and k_{10} = 9x10^{11}. For k_2 in MFM-180a-d_{16} E_2 = 28 kJ mol^{-1} and k_{20} = 3x10^{7}, while for MFM-181-d_{16} E_2 = 34 kJ mol^{-1} and k_{20} = 4.6x10^{8}. Additional analysis

suggests that intramolecular steric interactions in MFM-180a-d_{16} are stronger. In both cases these interactions are maximized when all phenyls lie in one plane, with three interaction sites and H-D or D-D distances governing the strength of interaction (Figures 5c,d). For MFM-180a-d_{16} Site I shows the interaction of two mobile phenyl groups in 1,1' positions of the ethylene core, while for MFM-181a-d_{16} it is the interaction of the mobile fragment with the hydrogen of the aromatic core fragment. Sites II and III are geometrically similar for both materials and the shortest distance is realized for site II (marked blue on Figures 5c,d). The rates of the slowest motion k_2 (Figure 6) are almost superimposable for both frameworks and we can thus attribute k_2 to the torsional barrier that rises from electrostatic interaction between neighboring hydrogens in site II. Hence the rate constant k_1 must be governed by site I because the shortest possible distance at the site III is d_3 ~ 1.9 Å and is identical in the two linkers, while for site I for MFM-180a-d_{16} d_1 ~ 1.6 Å and for the MFM-181a-d_{16} d_1 ~ 1.9 Å. The comparison of the first motion rates k_1 for the two materials confirms that they are indeed considerably different: k_1 is much greater in MFM-181-d_{16} than in MFM-180-d_{16}. Interestingly while the flipping mode k_1 in both cases is characterized by a collision factor typical for flipping motion in MOFs ~ 10^{11} Hz,[34] for k_2 it is ~ 3 orders of magnitude smaller at ~ 10^8 Hz, which reflects the strong influence of the steric restrictions on the axial rotation of the phenyl groups in these linkers. This ^{2}H NMR study has revealed the complex hierarchical dynamic behavior of the molecular rotors in MOFs in solid state, and there is a strong correlation between the ligand design and the rotational dynamics in MOFs, the latter of which is a key property of MOF functionalities.

CONCLUSIONS

The first series of octacarboxylate based MOF materials with controlled permanent porosity has been developed. The rigid, heteropolyaromatic linkers were designed to self-assemble with $[Cu_2(O_2CR)_4]$ paddlewheels to afford frameworks with elongated nano-tubular cages of fixed diameter. The isoreticular design results in systematically increased pore volumes and surface areas for the MOFs. Notably, in the case of CH_4 adsorption, extension of the linker causes no uptake loss in the low pressure region, and both gravimetric and volumetric uptakes are simultaneously enhanced at high pressure. This affords an impressive CH_4 "working capacity" of 0.24 g g^{-1} and 163 v/v (298 K, 5-65 bar) for activated MFM-185a. We attribute this behaviour to the efficient packing of gas molecules in the tubular pores and the high connectivity (and thus suitably high crystal density) of the framework. In addition, for the first time, a rational synthetic design has allowed control of the torsional dynamics of linkers in MOF solids. The high predictability of the linker/metal self-assembly combined with their pore shape make this series of MOFs a unique platform for exploring further the tuning of porosity, decoration of pores, and development and control of new molecular rotors in functional MOFs.

Methods Summary

MOFs preparation

The ligands H_8L^0, H_8L^1, H_8L^2, H_8L^3 and H_8L^5 were all synthesized using a Suzuki-Miyaura coupling reaction between the corresponding tetrahalogenated core and boronic acid, followed by hydrolysis of the ester functions. The synthesis of H_8L^1 is described in detail in SI. The selectively deuterated linkers were synthesised following the same procedures but starting from deuterated building blocks.

Synthesis of MFM-180, 181, 182, and 183: $H_8L^{0\text{-}3}$ (0.30 mmol) and $CuCl_2$ (0.19 g, 1.40 mmol) were dissolved in N,N'-diethylformamide (30 mL). EtOH (30 mL) and an aqueous solution of HCl (0.1M, 15 mL) were added to the resulting solution, which was placed in a tightly capped 250 mL Duran® pressure plus laboratory bottle (cat. n° 1092234). The solution was heated at 80 °C in an oven for 16 h, and a large amount of crystalline product precipitated. The crystal plates of the correspondind MOF were isolated by filtration while the mother liquor was still warm.

Solid state ^{2}H NMR spectroscopy

^{2}H NMR experiments were performed at 61.432 MHz on a Bruker Avance-400 spectrometer, using a high power probe with 5 mm horizontal solenoid coil. Metallic centers in the MOF structure are paramagnetic (Cu^{2+}, S = 1/2) which may influence the ^{2}H NMR spectrum by large frequency shifts and fast relaxation of the nuclear spin. To compensate these effects and correctly refocus the ^{2}H NMR spectrum an Exorcycled quadrupole-echo sequence was used, $(90_X - \tau_1 - 90_Y - \tau_2 - \mathrm{Acq} - t)$, where τ_1 = 20 μs, τ_2 = 22 μs, and t is a repetition time for the sequence during the accumulation of the NMR signal. The duration of the 90° pulses was 1.6 μs. To capture all dynamic features of the system, the measurements were performed over a broad temperature range, from 123 K to 523 K. 0.2 g of deuterated MOF sample was loaded in a 5 mm (o.d.) glass tube, connected to a vacuum system. The sample was heated at 373 K for 12 hours under a vacuum of 10^{-5} Torr. After cooling back to room temperature, the solid was sealed off by the flame while being kept at liquid nitrogen conditions to prevent overheating.

Detailed synthesis procedures and characterizations of the linkers and MOFs, along with crystallographic data (CCDC 1472806-1472810) and description of gas sorption, ^{2}H NMR experiments and spectra line shape simulation can be found in Supporting Information.

References

1. He Y, Zhou W, Qian G, Chen B (2014) Methane storage in metal–organic frameworks. *Chem Soc Rev* 43:5657-5678.

2. Zhang Z, Yao Z, Xiang S, Chen B (2014) Perspective of microporous metal–organic frameworks for CO_2 capture and separation. *Energy Environ Sci* 7:2868.

3. Yang S et al. (2012) Selectivity and direct visualization of carbon dioxide and sulfur dioxide in a decorated porous host. *Nature Chem* 4:887-894.

4. Horcajada P et al. (2012) Metal–organic frameworks in biomedicine. *Chem Rev* 112:1232-1268.

5. Lee J et al. (2009) Metal–organic framework materials as catalysts. *Chem Soc Rev* 38:1450.

6. Li J, Sculley J, Zhou H (2012) Metal–organic frameworks for separations. *Chem Rev* 112:869-932.

7. Mondloch J et al. (2015) Destruction of chemical warfare agents using metal–organic frameworks. *Nature Mater* 14:512-516.

8. Li M, Li D, O'Keeffe M, Yaghi O (2014) Topological analysis of metal–organic frameworks with polytopic linkers and/or multiple building units and the minimal transitivity principle. *Chem Rev* 114:1343-1370.

9. Alsmail N et al. (2014) Analysis of high and selective uptake of CO_2 in an oxamide-containing {$Cu_2(OOCR)_4$}-based metal-organic framework. *Chem Euro J* 20:7317-7324.

10. Yang S et al. (2014) Supramolecular binding and separation of hydrocarbons within a functionalized porous metal–organic framework. *Nature Chem* 7:121-129.

11. Lin X, Champness N, Schröder M (2010) Hydrogen, methane and carbon dioxide adsorption in metal-organic framework materials. *Top Curr Chem*:35-76.

12. Batten S, Robson R (1998) Interpenetrating nets: ordered, periodic entanglement. *Angew Chem Int Ed* 37:1460-1494.

13. Haldar R, Sikdar N, Maji T (2015) Interpenetration in coordination polymers: structural diversities toward porous functional materials. *Mater Today* 18:97-116.

14. Lin X et al. (2009) High capacity hydrogen adsorption in Cu(II) tetracarboxylate framework materials: the role of pore size, ligand functionalization, and exposed metal sites. *J Am Chem Soc* 131:2159-2171.

15. Yan Y et al. (2009) Exceptionally high H_2 storage by a metal–organic polyhedral framework. *Chem Commun*:1025-1028.

16. Nouar F et al. (2008) Supermolecular building blocks (SBBs) for the design and synthesis of highly porous metal-organic frameworks. *J Am Chem Soc* 130:1833-1835.

17. Farha O et al. (2012) Metal–organic framework materials with ultrahigh surface areas: is the sky the limit?. *J Am Chem Soc* 134:15016-15021.

18. Tan C et al. (2011) High capacity gas storage by a 4,8-connected metal–organic polyhedral framework. *Chem Commun* 47:4487.

19. Ma L, Mihalcik D, Lin W (2009) Highly porous and robust 4,8-connected metal−organic frameworks for hydrogen storage. *J Am Chem Soc* 131:4610-4612.

20. Mihalcik D, Zhang T, Ma L, Lin W (2012) Highly porous 4,8-connected metal–organic frameworks: synthesis, characterization, and hydrogen uptake. *Inorg Chem* 51:2503-2508.

21. Eubank J et al. (2011) The quest for modular nanocages: tbo-MOF as an archetype for mutual substitution, functionalization, and expansion of quadrangular pillar building blocks. *J Am Chem Soc* 133:14204-14207.

22. Xue Y et al. (2012) Structural diversity and properties of coordination polymers built from a rigid octadentenate carboxylic acid. *Cryst Growth Des* 12:6158-6164.

23. Zhuang W et al. (2012) Robust metal–organic framework with an octatopic ligand for gas adsorption and separation: combined characterization by experiments and molecular simulation. *Chem Mater* 24:18-25.

24. Wei Z, Lu W, Jiang H, Zhou H (2013) A route to metal–organic frameworks through framework templating. *Inorg Chem* 52:1164-1166.

25. Lu W, Yuan D, Makal T, Li J, Zhou H (2012) A highly porous and robust (3,3,4)-connected metal-organic framework assembled with a 90° bridging-angle embedded octacarboxylate ligand. *Angew Chem Int Ed* 51:1580-1584.

26. Spanopoulos I et al. (2016) Reticular synthesis of HKUST-like tbo-MOFs with enhanced CH_4 storage. *J Am Chem Soc* 138:1568-1574.

27. Kolokolov D et al. (2010) Dynamics of benzene rings in MIL-53(Cr) and MIL-47(V) frameworks studied by ^{2}H NMR Spectroscopy. *Angew Chem Int Ed* 49:4791-4794.

28. Gould S, Tranchemontagne D, Yaghi O, Garcia-Garibay M (2008) Amphidynamic character of crystalline MOF-5: rotational dynamics of terephthalate phenylenes in a free-volume, sterically unhindered environment. *J Am Chem Soc* 130:3246-3247.

29. Kolokolov D, Stepanov A, Jobic H (2014) Guest controlled rotational dynamics of terephthalate phenylenes in metal–organic framework MIL-53(Al): effect of different xylene loadings. *J Phys Chem C* 118:15978-15984.

30. Horike S et al. (2006) Dynamic motion of building blocks in porous coordination polymers. *Angew Chem Int Ed* 45:7226-7230.

31. Comotti A, Bracco S, Ben T, Qiu S, Sozzani P (2014) Molecular rotors in porous organic frameworks. *Angew Chem Int Ed* 126:1061-1065.

32. Delgado-Friedrichs O, O'Keeffe M, Yaghi O (2006) Three-periodic nets and tilings: edge transitive binodal structures. *Acta Cryst Sect A* 62:350-355.

33. Macho V, Brombacher L, Spiess H (2001) The NMR-WEBLAB: an internet approach to NMR lineshape analysis. *Appl Magn Reson* 20:405-432.

Corresponding Author

Sihai.Yang@manchester.ac.uk; M.Schroder@manchester.ac.uk

Author Contributions

FM: syntheses, characterization of ligands and MOFs. FM and AD: measurements of gas adsorption isotherms. FM, TLE, WL, AJB and HN: collection and analysis of the single-crystal X-ray data. DIK and AGS: solid-state ^{2}H NMR measurements. MJL and EB: modelling of isotherms. SY and MS: overall direction of the project. FM, DIK, SY and MS: preparation of the paper with contributions from all authors.

Acknowledgments

We thank the EPSRC, ERC, the Universities of Nottingham and the University of Manchester for funding, and the access to the High Performance Computing (HPC) Facility at University of Nottingham. MS gratefully acknowledges the Russian Ministry of Science and Education for the award of a Russian Megagrant, and the ERC for an Advanced Grant. MS and KDI gratefully acknowledge receipt of the Royal Society International Exchanges Scheme grant ref. IE150114. We thank Diamond Light Source for the access to beamline I19.

Competing financial interests

The authors declare no competing financial interests.

Schemes and Figures

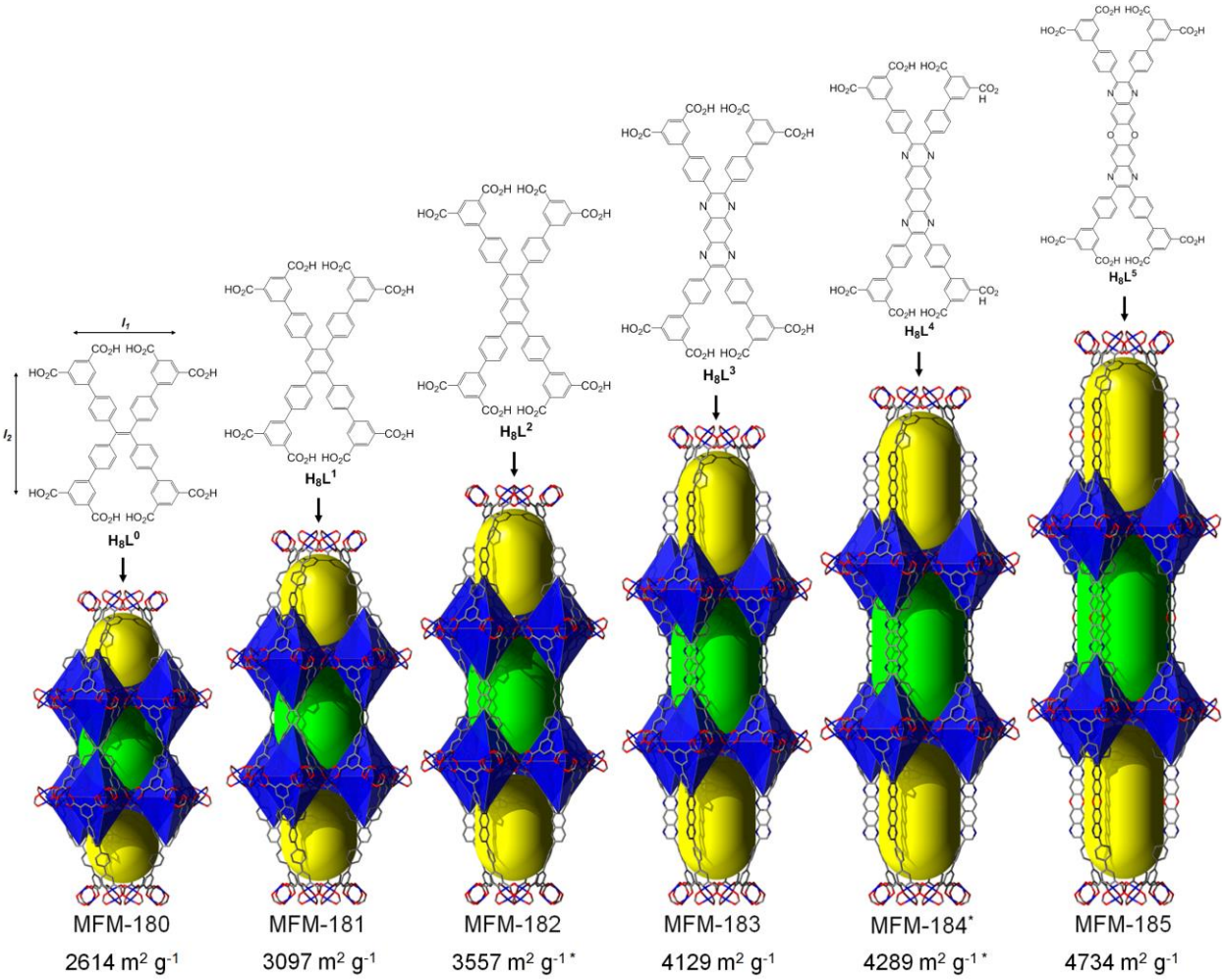

Figure 1. Chemical structures for the octacarboxylate linkers H_8L^0 to H_8L^5 used for the synthesis of MFM-180 to MFM-185, representation of the cage assembly in MFM-180, MFM-181, MFM-182, MFM-183, MFM-184 (*predicted structure) and MFM-185, and corresponding BET surface areas (*obtained from modelling).

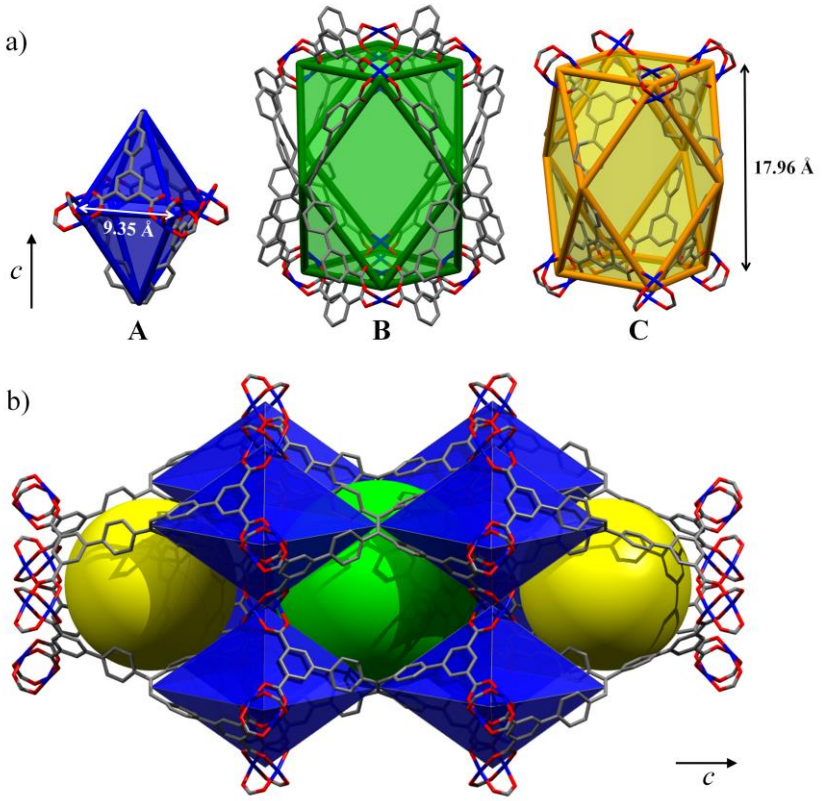

Figure 2. View of a) polyhedral representations of the three types of cages A (octahedral), B and C (cuboctahedral) and b) their three-dimensional assembly in MFM-180.

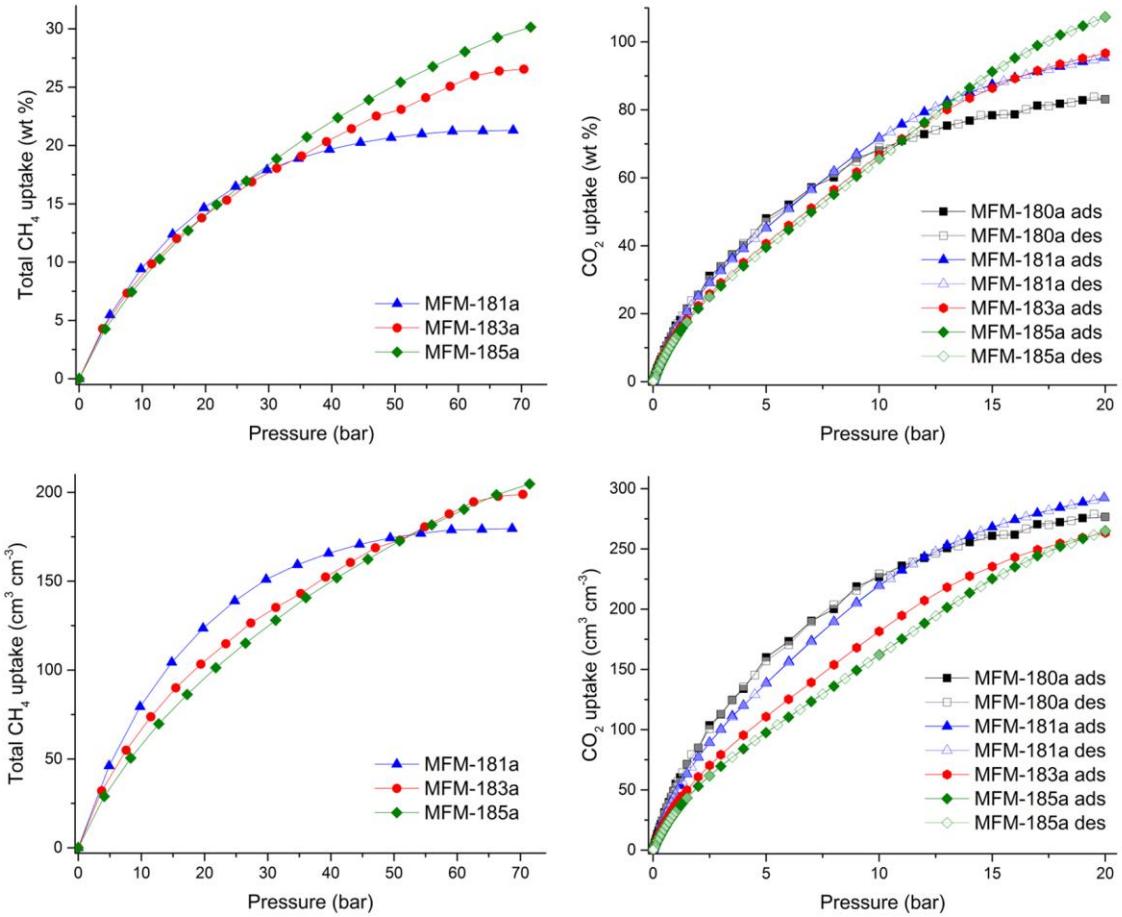

Figure 3. High pressure CH_4 sorption isotherms for MFM-181a, -183a and -185a at 298 K and CO_2 sorption isotherms for MFM-180a, -181a, -183a and -185a up to 20 bar at 298 K. Top: gravimetric uptake; bottom: volumetric uptake.

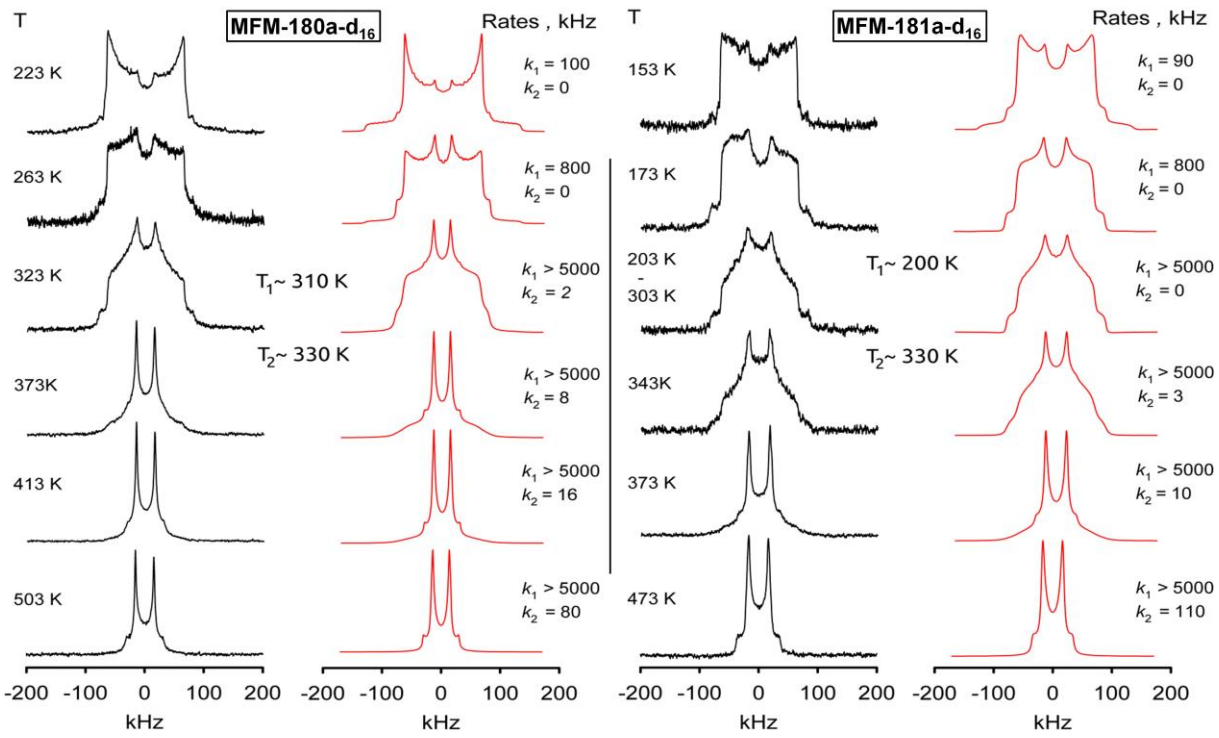

Figure 4. Comparison of the ^{2}H NMR line shape temperature dependence for phenyl fragments in MFM-180a-d_{16} and MFM-181a-d_{16} (experimental – black, simulation - red).

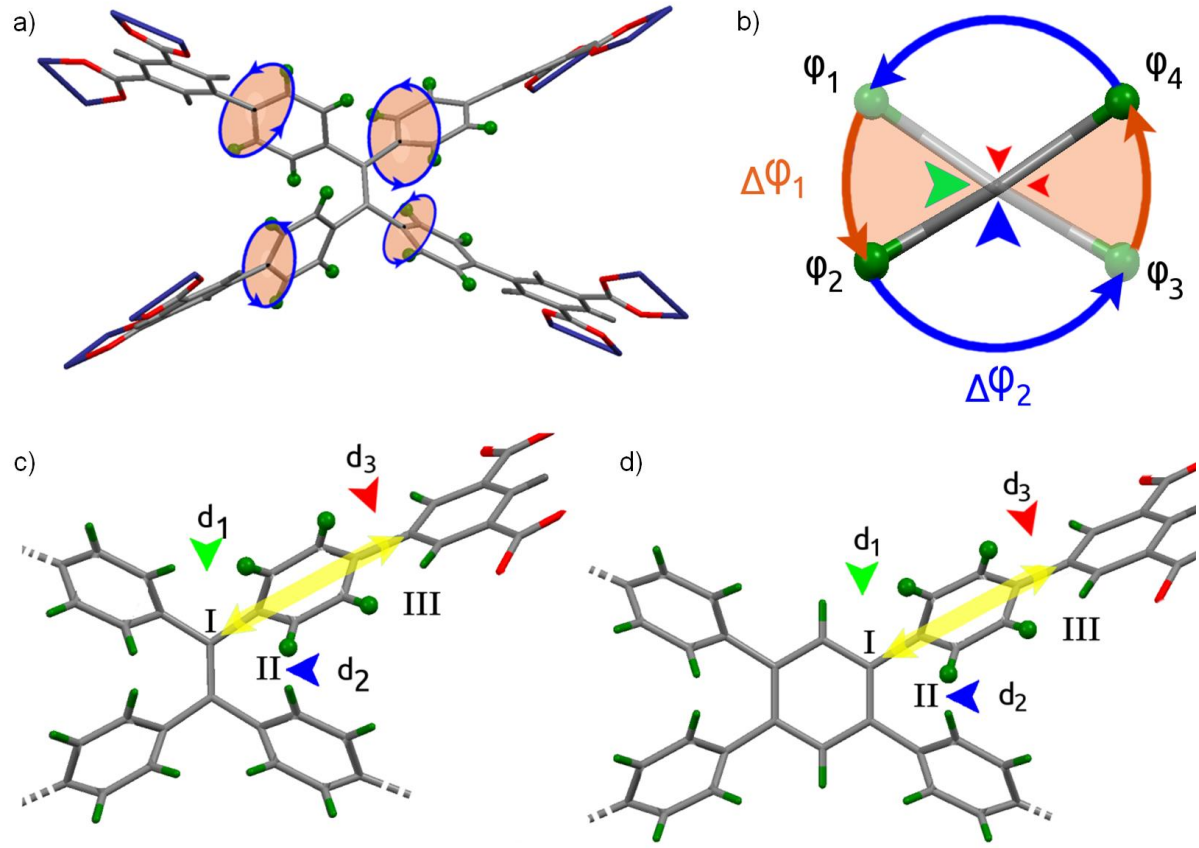

Figure 5. a) Representation of the linker in MFM-180a-d_{16} with its four mobile phenyl rings; b) Scheme of rotation sites for phenyl groups in MFM-180a-d_{16} and MFM-181a-d_{16}. The reorientation scheme comprises a four site exchange motion with two different rate constants: k_1 ($\Delta\varphi_1$) and k_2 ($\Delta\varphi_2$). The green arrow represents the barrier associated with k_1, the blue arrow represents the barrier associated with k_2, and the red arrows are associated with barriers in the $\Delta\varphi_1$ and $\Delta\varphi_2$ regions associated with minor steric restrictions. c) and d) Scheme of interaction sites that might influence the rotational potential for phenyl groups in MFM-180a-d_{16} and MFM-181a-d_{16}, respectively. Parameter d_2 is the shortest achievable distance for the electrostatic interaction between the phenyl hydrogens and is similar in both materials.

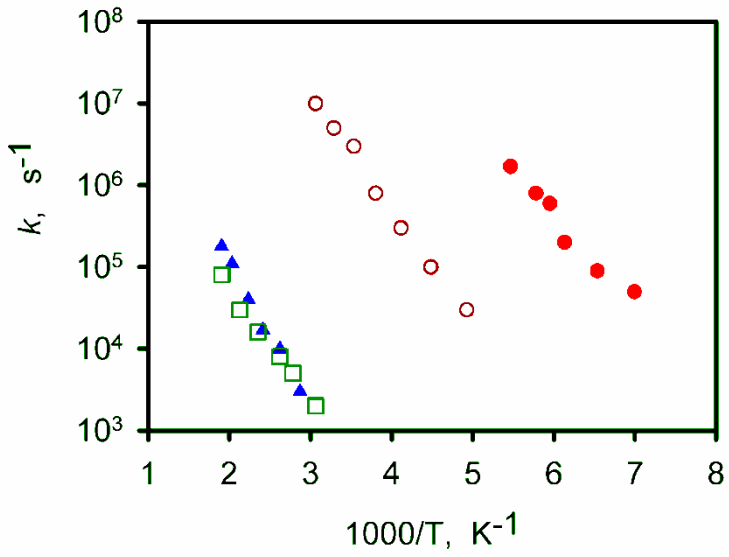

Figure 6. Arrhenius plots of the rotational rate constants k : (○) k_1 and (□) k_2 for MFM-180a-d_{16}; (●) k_1 and (▲) k_2 for MFM-181a-d_{16}.

SUPPORTING INFORMATION

Tailoring Porosity and Rotational Dynamics in a Series of Octacarboxylate Metal-Organic Frameworks

Florian Moreau,[a] Daniil I. Kolokolov,[b,c] Alexander G. Stepanov,[b,c] Timothy L. Easun,[d] Anne Dailly,[e] William Lewis,[f] Alexander J. Blake,[f] Harriott Nowell,[g] Matthew J. Lennox,[f] Elena Besley,[f] Sihai Yang[a]* and Martin Schröder[a,h]*

[a] School of Chemistry, University of Manchester, Oxford Road, Manchester M13 9PL, UK.

[b] Boreskov Institute of Catalysis, Siberian Branch of Russian Academy of Sciences, Prospekt Akademika Lavrentieva 5, Novosibirsk 630090, Russia.

[c] Novosibirsk State University, Pirogova Street 2, Novosibirsk 630090, Russia.

[d] School of Chemistry, Cardiff University, Main Building, Park Place, Cardiff CF10 3AT, UK.

[e] General Motors Global Research and Development Center, Warren, MI, USA

[f] School of Chemistry, University of Nottingham, University Park, Nottingham NG7 2RD, UK.

[g] Diamond Light Source, Harwell Science Campus, Oxon, OX11 0DE, UK.

[h] Nikolaev Institute of Inorganic Chemistry, Siberian Branch of the Russian Academy of Sciences, 3 Acad. Lavrentiev Ave., Novosibirsk, 630090, Russia.

Experimental Section

All chemical reagents and gases were obtained from commercial sources and unless otherwised noted used without further purification. 2-(4-Bromophenyl)-2,3-dihydro-1H-naphtho[1,8-de][1,3,2]diazaborinine, 1,1,2,2-tetrakis(4-bromophenyl)ethane, 3,5-bis(ethoxycarbonyl)phenylboronic acid, 2,3,6,7-tetraiodonaphthalene and dibenzo[b,e][1,4]dioxine-2,3,7,8-tetraamine tetrahydrochloride salt were prepared according to previously published procedures.[1–5] ^{1}H and ^{13}C NMR were measured on Bruker DPX 300, Bruker AV400, or Bruker AV(III)500 spectrometers. Residual protonated species in the deuterated solvents were used as internal references. Mass spectrometry was performed on a Bruker MicroTOF with the sample dissolved in methanol or acetonitrile. MALDI was performed on a Bruker Ultraflex III spectrometer and analysed using Flex Analysis software. Elemental analyses were measured on a CE-440 Elemental Analyzer provided by Departmental Analytical Services at the Universities of Nottingham and Manchester.

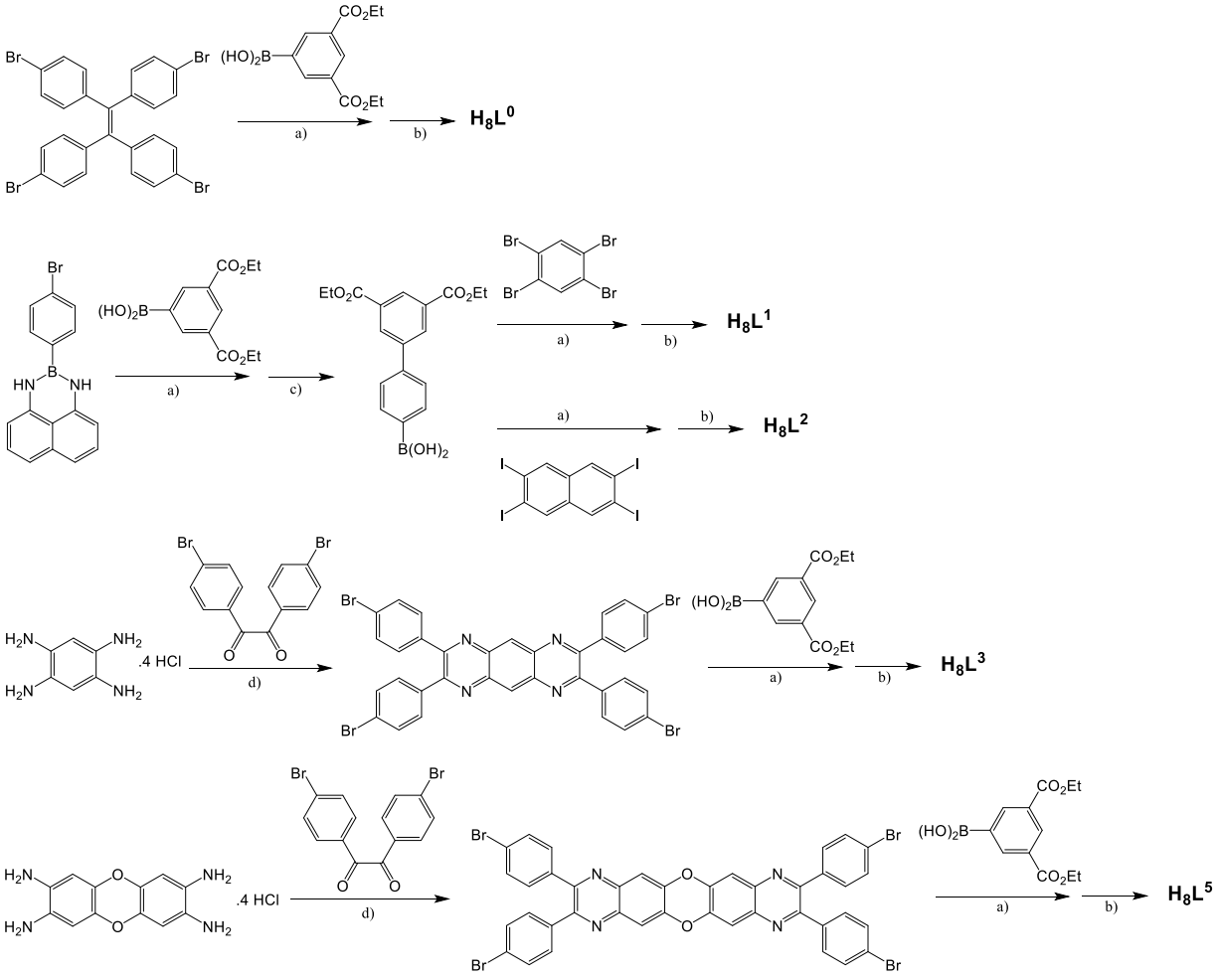

Scheme S1. Synthesis of linkers. Reagents and conditions: a) Pd_2dba_3, $P(^tBu)_3$, K_2CO_3, toluene/water, 80 °C, 1 h; b) NaOH, THF, EtOH, H_2O, 80 °C, 16 h; c) H_2SO_4, THF, H_2O, 80 °C, 16 h; d) 2-iodoxybenzoic acid, $MeCO_2H$, 120 °C, 16 h.

Preparation of 3',5'-bis(ethoxycarbonyl)biphenyl-4-ylboronic acid. 2-(4-Bromophenyl)-2,3-dihydro-1*H*-naphtho[1,8-*de*][1,3,2]diazaborinine (4.0 g, 12.4 mmol), 3,5-bis(ethoxycarbonyl)phenylboronic acid (3.8 g, 14.28 mmol) and K_2CO_3 (2.5 g, 18.1 mmol) were added to a mixture of toluene and deionized water (500 mL; 4:1 v/v). The resulting suspension was degassed under Ar for 20 min and heated at 60 °C. While stirring at 60 °C under Ar, tri-*tert*-butylphosphine (1M in toluene, 3.0 mL) and [$Pd_2(dba_3)$] (dba = dibenzylideneacetone) (1.0 g, 1.09 mmol) were added sequentially. After addition, the reaction was heated to 80 °C for 1 h. The resulting mixture was filtered while hot and once cooled to room temperature the filtrate was extracted with CH_2Cl_2 (3 × 150 mL). The combined extracts were dried over $MgSO_4$ and the solvent removed *in vacuo*. Recrystallization from CH_2Cl_2/hexane afforded diethyl 4'-(1*H*-naphtho[1,8-*de*][1,3,2]diazaborinin-2(3*H*)-yl)biphenyl-3,5-dicarboxylate as a yellow solid which was dissolved in THF (400 mL), aqueous H_2SO_4 (2M, 70 mL) was added and the solution refluxed for 16 h. The resulting suspension was filtered and the precipitate discarded. The filtrate was concentrated *in vacuo* to 100 mL and deionized H_2O added to the residue to precipitate the product. The white solid was isolated by filtration, thoroughly washed with deionized water, and dried. Yield: 3.1 g, 72 %. ^{1}H NMR: (300 MHz, DMSO-d_6) δ/ppm = 8.42 (t, *J* = 1.5 Hz, 1H, ArH), 8.38 (d, *J* = 1.6 Hz, 2H, ArH), 7.93 (d, *J* = 8.2 Hz, 2H, ArH), 7.69 (d, *J* = 8.2 Hz, 2H, ArH), 4.38 (q, *J* = 7.1 Hz, 4H, Et), 1.35 (t, *J* = 7.1 Hz, 6H, Me); ^{13}C NMR: (75 MHz, $CDCl_3$), δ/ppm = 166.9 (C), 140.9 (C), 140.7 (C), 139.2 (C), 137.3 (C), 132.6 (CH), 131.6 (CH), 131.0 (CH), 129.2 (C), 128.5 (CH), 127.3 (CH); MS: (ESI) Calcd: 343.134 Found: 343.135 (100 %) $[MH]^+$.

Preparation of 2,3,7,8-tetrakis(4-bromophenyl)pyrazino[2,3-*g*]quinoxaline. 1,2,4,5-Tetraaminobenzene tetrahydrochloride (0.5 g, 1.76 mmol), 4,4'-dibromobenzil (1.30 g, 3.52 mmol) and 2-iodoxybenzoic acid (45 wt%, 18.3 mg, 0.03 mmol) were dissolved in glacial acetic acid (70 mL). The resulting solution was heated to reflux for 16 h and then cooled. Upon addition of deionized H_2O the product precipitated as a yellow solid, which was isolated by filtration, washed with H_2O then EtOH, and dried in air. Yield: 1.158 g, 82 %; ^{1}H NMR: (400 MHz, CF_3CO_2D) δ/ppm = 9.70 (s, 2H, ArH), 7.90 (d, *J* = 8.8 Hz, 8H, ArH), 7.73 (d, *J* = 8.6 Hz, 8H, ArH); ^{13}C NMR: (100 MHz, CF_3CO_2D), δ/ppm = 156.8 (C), 136.5 (C), 132.9 (C), 131.4 (CH), 130.5 (CH), 129.8 (CH), 123.5 (C); MS: (APCI) Calcd: 802.829 Found: 802.828 $[MH]^+$.

Preparation of [1,4]Dioxino[2,3-*g*:5,6-*g*']diquinoxaline-2,3,9,10-tetra-4-bromophenyl. Dibenzo[b,e][1,4]dioxine-2,3,7,8-tetraamine tetrahydrochloride salt (860 mg, 2.20 mmol), 4,4'-dibromobenzil (1.62 g, 4.40 mmol) and 2-iodoxybenzoic acid (stabilized, 45 wt%, 54 mg, 0.09 mmol) were dissolved in glacial acetic acid (125 mL). The resulting solution was heated to reflux for 16 h then allowed to cool. Upon addition of deionized H_2O the product precipitated, was isolated by filtration, washed with water then EtOH, and dried to yield brown solid. Yield: 1.725 g, 86%. ^{1}H NMR: (400 MHz, CF_3CO_2D) δ/ppm = 8.23 (s, 4H, ArH), 7.76 (d, *J* = 8.5 Hz, 8H, ArH), 7.52 (d, *J* = 8.5 Hz, 8H, ArH); ^{13}C NMR: (125 MHz, CF_3CO_2D), δ/ppm = 151.2 (C), 146.3 (C), 135.5 (C), 132.8

(C), 130.9 (CH), 129.9 (CH), 128.4 (C), 109.2 (CH); MS (MALDI-TOF, dithranol matrix, positive mode) Calcd: 908.8 Found: 908.9 $[MH]^+$.

Preparation of ligands

The ligands H_8L^0, H_8L^1, H_8L^2, H_8L^3 and H_8L^5 (H_8L^0 = 4',4''',4'''',4'''''-(ethene-1,1,2,2-tetrayl)tetrakis(([1,1'-biphenyl]-3,5-dicarboxylic acid)), H_8L^1 = 4',4''',4'''',4'''''-(benzene-1,2,4,5-tetrayl)tetrakis(([1,1'-biphenyl]-3,5-dicarboxylic acid)), H_8L^2 = 4',4''',4'''',4'''''-(naphthalene-2,3,6,7-tetrayl)tetrakis(([1,1'-biphenyl]-3,5-dicarboxylic acid)), H_8L^3 = 4',4''',4'''',4'''''-(pyrazino[2,3-g]quinoxaline-2,3,7,8-tetrayl)tetrakis(([1,1'-biphenyl]-3,5-dicarboxylic acid)), H_8L^5 = 4',4''',4'''',4'''''-([1,4]dioxino [2,3-*g*:5,6-*g*']diquinoxaline-2,3,9,10-tetrayl)tetrakis(([1,1'-biphenyl]-3,5-dicarboxylic acid))) were all synthesized using a Suzuki-Miyaura coupling reaction between the corresponding tetrahalogenated core and boronic acid, followed by hydrolysis of the ester functions. The synthesis of H_8L^1 is described in detail.

Preparation of H_8L^1. 1,2,4,5-Tetrabromobenzene (0.3 g, 0.76 mmol), 3',5'-bis(ethoxycarbonyl)biphenyl-4-ylboronic acid (1.1 g, 3.21 mmol) and K_2CO_3 (0.45 g, 3.26 mmol) were added to a mixture of toluene and deionized H_2O (150 mL; 4:1 v/v) and the resulting suspension was degassed under Ar for 20 min and then heated to 60 °C. While stirring at 60 °C under Ar, P(*t*-Bu)$_3$ (1M in toluene, 0.5 mL) and then [$Pd_2(dba)_3$] (0.18 g, 0.2 mmol) were added. The reaction mixture was heated to 80 °C for 1 h under Ar. The resultant mixture was filtered through a sintered funnel while hot and once cooled to room temperature the filtrate was extracted with CH_2Cl_2 (3 × 100 mL). The combined extracts were dried over $MgSO_4$, and the solvent removed *in vacuo*. The residue was re-dissolved in CH_2Cl_2 (50 mL) and the octa-ethyl ester of the target ligand was precipitated by addition of hot MeOH (100 mL) and isolated by filtration while hot (0.7 g, 73%) as an off white solid. The ester was dissolved in THF and EtOH (200 mL; 1:1 v/v), an aqueous solution of NaOH (2M, 100 mL) added, and the mixture refluxed for 16 h. The resultant solution was concentrated *in vacuo* to 100 mL and acidified to pH 2-3 using concentrated hydrochloric acid. The precipitate was isolated by filtration, thoroughly washed with water, and recrystallized from N,N'-dimethylformamide/H_2O to afford pure H_8L^1 as a white solid. Yield: 0.52 g, 90 %. ^{1}H NMR: (400 MHz, DMSO-d6), δ/ppm = 13.37 (sbr, 8H, COOH), 8.44 (s, 4H, ArH), 8.39 (s, 8H, ArH), 7.73 (d, J = 8.3 Hz, 8H, ArH), 7.63 (s, 2H, ArH), 7.48 (d, J = 8.3 Hz, 8H, ArH); ^{13}C NMR: (100 MHz, DMSO-d6), δ/ppm = 166.9 (C), 140.9 (C), 140.7 (C), 139.2 (C), 137.3 (C), 132.6 (CH), 131.6 (CH), 131.0 (CH), 129.2 (C), 128.5 (CH), 127.3 ppm (CH); MS (ESI) Calcd: 1037.209 Found: 1037.203 $[M-H]^-$.

H_8L^0. ^{1}H NMR: (400 MHz, DMSO-d6), δ/ppm = 13.27 (sbr, 8H, COOH), 8.41 (s, 4H, ArH), 8.34 (s, 8H, ArH), 7.63 (d, J = 8.1 Hz, 8H, ArH), 7.24 (d, J = 8.1 Hz, 8H, ArH); ^{13}C NMR: (100 MHz, DMSO-d6), δ/ppm = 167.0 (C), 143.5 (C), 141.9 (C), 140.7 (C), 137.0 (C), 132.6 (C), 132.5 (CH), 131.5 (CH), 129.3 (CH), 126.9 ppm (CH); MS (ESI) Calcd: 987.293 Found 987.282 $[M-H]^-$

H_8L^2. ^{1}H NMR: (400 MHz, DMSO-d6), δ/ppm = 13.35 (sbr, 8H, COOH), 8.43 (s, 4H, ArH), 8.37 (s, 8H, ArH), 7.71 (d, J = 8.3 Hz, 8H, ArH), 7.58 (s, 4H, ArH), 7.44 (d, J = 8.3 Hz, 8H, ArH); ^{13}C NMR:

(100 MHz, DMSO-d6), δ/ppm = 166.9 (C), 141.3 (C), 140.8 (C), 138.7 (C), 137.1 (C), 132.5 (C), 131.6 (CH), 131.0 (CH), 130,1(CH), 129.3 (CH), 128.1 (C), 127.1 ppm (CH); MS (ESI) Calcd: 1087.223 Found 1087.227 $[M-H]^-$

H_8L^3. ^{1}H NMR: (400 MHz, DMSO-d6), δ/ppm = 13.39 (sbr, 8H, COOH), 8.89 (s, 2H, ArH), 8.44 (s, 4H, ArH), 8.39 (s, 8H, ArH), 7.80 (d, J = 8.2 Hz, 8H, ArH), 7.76 (d, J = 8.2 Hz, 8H, ArH); ^{13}C NMR: (100 MHz, DMSO-d6), δ/ppm = 166.8 (C), 154.8 (C), 140.5 (C), 140.2 (C), 139.6 (C), 138.6 (C), 132.5 (CH), 131.7 (CH), 131.3 (CH), 129.6 (CH), 128.4 (CH), 127.1 ppm (CH); MS (APCI) Calcd: 1143.236 Found: 1143.238 $[MH]^+$)

H_8L^5. ^{1}H NMR: (400 MHz, CF_3CO_2D), δ/ppm = 9.05 (s, 4H, ArH), 8.82 (s, 8H, ArH), 8.33 (s, 4H, ArH), 8.01 (d, J = 7.2 Hz, 8H, ArH), 7.94 (d, J = 7.4 Hz, 8H, ArH); ^{13}C NMR: (125 MHz, CF_3CO_2D), δ/ppm = 171.2 (C), 151.6 (C), 146.4 (C), 143.0 (C), 140.9 (C), 135.7 (C), 134.0 (CH), 131.7 (C), 130.8 (CH), 130.2 (CH), 129.9 (CH), 128.0 (C), 109.1 ppm (CH); MS (APCI) Calcd: 1249.241 Found: 1249.240 [MH]+)

Preparation of selectively deuterated linkers

The deuterated linkers were synthesised following the same procedures as above but starting from deuterated building blocks: 1,1,2,2-tetrakis(4-bromophenyl)ethane-d_{16} and 2,3-dihydro-1H-naphtho[1,8-de][1,3,2]diazaborinine-d_4 which were synthesised as previously reported.[1,6]

d_{16}-H_8L^0. ^{1}H NMR: (400 MHz, DMSO-d_6), δ/ppm = 13.35 (sbr, 8H, COOH), 8.42 (s, 4H, ArH), 8.33 (s, 8H, ArH); ^{13}C NMR: (100 MHz, DMSO-d_6), δ/ppm = 166.9 (C), 143.3 (C), 140.5 (C), 140.6 (C), 136.7 (C), 132.5 (C), 131.7 (CD), 131.4 (CH), 129.2 (CH), 126.4 ppm (CD); MS(ESI) Calcd: 1003.294 Found: 1003.287 (100 %) $[M-H]^-$.

d_{16}-H_8L^1. ^{1}H NMR: (400 MHz, DMSO-d_6), δ/ppm = 13.36 (sbr, 8H, COOH), 8.43 (s, 4H, ArH), 8.37 (s, 8H, ArH), 7.61 (s, 2H, ArH); ^{13}C NMR: (100 MHz, DMSO-d_6), δ/ppm = 166.9 (C), 140.8 (C), 140.5 (C), 139.1 (C), 137.1 (C), 133.4 (CH), 132.5 (C), 131.6 (CH), 130.53 (CD), 129.3 (CH), 126.8 ppm (CD); MS (ESI) Calcd: 1053.3091 Found: 1053.3028 (100 %) $[M-H]^-$.

Preparation of MOF materials

Yields were calculated based on TGA of the as-synthesized materials since the precise solvent content within the pores is variable, rendering evaluation by means of elemental analysis can thus be problematic. Therefore, elemental analyses of materials were performed after activation of the materials and re-hydration upon exposure under standard conditions so that the exact water content of the framework could be evaluated by TGA.

Preparation of MFM-180:

H_8L^0 (0.30 g, 0.30 mmol) and $CuCl_2$ (0.19 g, 1.40 mmol) were dissolved in N,N'-diethylformamide (30 mL). EtOH (30 mL) and an aqueous solution of HCl (0.1M, 15 mL) were added to the resulting solution, which was placed in a tightly capped 250 mL Duran® pressure plus laboratory bottle (cat. n° 1092234). The solution was heated at 80 °C in an oven for 16 h, and a large amount of crystalline

product precipitated. The blue crystal plates were isolated by filtration while the mother liquor was still warm and washed sequentially with warm DMF and MeOH and then dried in air (yield: 0.52 g, 79 %). After activation and rehydration, $[Cu_4(L^0)(H_2O)_4]\cdot 7H_2O$ was obtained; elemental analysis: Calcd: C, 48.61; H, 3.52; Found: C, 48.93; H, 3.20 %.

Preparation of MFM-181:

H_8L^1 (0.31 g, 0.30 mmol) and $CuCl_2$ (0.19 g, 1.40 mmol) were dissolved in N,N'-diethylformamide (30 mL). EtOH (30 mL) and an aqueous solution of HCl (0.1M, 15 mL) were added to the resulting solution, which was placed in a tightly capped 250 mL Duran® pressure plus laboratory bottle. The solution was heated at 80 °C in an oven for 16 h, and a large amount of crystalline product precipitated. The large blue plate-shaped crystals were isolated by filtration while the mother solution was still warm and washed sequentially with warm DMF and MeOH, then dried in air (yield: 0.48 g, 68 %). After activation and rehydration, $[Cu_4(L^1)(H_2O)_4]\cdot 11H_2O$ was obtained; elemental analysis: Calcd: C, 47.88; H, 3.89; Found: C, 47.95; H, 3.90 %.

Preparation of MFM-182:

H_8L^2 (0.010 g, 0.009 mmol) and $CuCl_2$ (0.006 g, 0.045 mmol) were dissolved in N,N'-diethylformamide (1 mL). EtOH (1 mL) and an aqueous solution of HCl (0.1M, 0.5 mL) were added to the resulting solution, which was placed in a tightly capped 8 mL Pyrex vial. The solution was heated at 80 °C in an oven for 16 h, and blue plate-shaped crystals precipitated.

Preparation of MFM-183:

H_8L^3 (0.34 g, 0.30 mmol) and $CuCl_2$ (0.19 g, 1.40 mmol) were dissolved in N,N'-diethylformamide (30 mL). EtOH (30 mL) and an aqueous solution of HCl (0.1M, 15 mL) were added to the resulting solution, which was placed in a tightly capped 250 mL Duran® pressure plus laboratory bottle. The solution was heated at 80 °C in an oven for 16 h, and a large amount of crystalline product precipitated. The large green plate-shaped crystals were isolated by filtration while the mother solution was still warm and washed sequentially with warm DMF and MeOH, then dried in air (yield: 0.56 g, 75 %). After activation and rehydration, $[Cu_4(L^3)H_2O)_4]\cdot 12H_2O$ was obtained; elemental analysis: Calcd: C, 47.26; H, 3.73; N, 3.34; Found: C, 48.75; H, 3.33; N, 3.49 %.

Preparation of MFM-185:

H_8L^5 (0.125 g, 0.10 mmol) and $Cu(NO_3)_2\cdot 2.5H_20$ (0.50 g, 2,15 mmol) were dissolved in DMSO (25 mL). *N*,*N'*-Dimethylformamide (50 mL) and an aqueous solution of HCl (2M, 1.25 mL) were added to the resulting solution, which was placed in a tightly capped 250 mL Duran® pressure plus laboratory bottle. The solution was heated at 80°C in an oven for 5 days, and a large amount of crystalline product precipitated. The green plate-shaped crystals were isolated by filtration while the mother solution was still warm and washed sequentially with hot DMSO and MeOH, then dried in air (yield: 0.45 g, 71 %). After activation and rehydration, $[Cu_4(L^5)(H_2O)_4]\cdot 10H_2O$ was obtained; elemental analysis: Calcd: C, 49.49; H, 3.46; N, 3.09; Found: C, 48.65; H, 3.01; N, 3.23 %.

Preparation of selectively deuterated MOFs

The deuterated MOFs were synthesised following the same procedures starting from deuterated linkers

X-ray Crystallography

Single crystal X-ray diffraction structure determinations

Single crystal diffraction datasets for MFM-180, MFM–181 and MFM-182 were collected at 120 K using an Agilent GV1000 diffractometer, and for MFM-183 and MFM-185 using synchrotron radiation on Beamline I19 at Diamond Light Source. Details of data collection and processing procedures are included in the CIF files. Structures were solved by direct methods using SHELXS[7] and remaining atoms were localised from successive difference Fourier maps using SHELXL.[8] The hydrogen atoms from the linkers and the coordinating water molecules were placed geometrically and refined using a riding model. The refinement of the framework was performed by ignoring the contribution of the disordered solvent molecules. The region containing the disordered electron density was identified by considering the van der Waals radii of the atoms constituting the ordered framework. The contribution of this region to the total structure factor was calculated via a discrete Fourier transformation and subtracted in order to generate a new set of *hkl* reflections by means of the program SQUEEZE.[9]

Table S1. Crystal data and structure refinement details for MFM-180

Identification code	MFM-180
Chemical formula	$(C_{58}H_{36}Cu_4O_{20})$
M_r (g mol^{-1})	2178.21
Crystal system, space group	Tetragonal, $I\bar{4}2m$
Temperature (K)	120
a, *c* (Å)	18.69242 (16), 35.9196 (4)
V (Å^3)	12550.6 (2)
Z	4
Radiation type	Cu *K*α
μ (mm^{-1})	1.38
Crystal size (mm)	0.09 × 0.07 × 0.03
Absorption correction	Gaussian .
T_{min}, T_{max}	0.911, 0.965
No. of measured, independent and observed [$I > 2s(I)$] reflections	36516, 6651, 6228
R_{int}	0.035
(sin θ/ λ)max (Å-1)	0.626
$R[F^2 > 2s(F^2)]$, $wR(F^2)$, *S*	0.029, 0.083, 1.04
No. of reflections	6651
No. of parameters	195
H-atom treatment	H-atom parameters constrained
$D\rho_{max}$, $D\rho_{min}$ (e Å^{-3})	0.48, -0.20
Absolute structure	Refined as an inversion twin.
Absolute structure parameter	0.64 (3)

Table S2. Crystal data and structure refinement details for MFM-181

Identification code	MFM-181
Chemical formula	$(C_{62}H_{38}Cu_4O_{20})$
M_r	2556.59
Crystal system, space group	Tetragonal, *I*4/*mmm*
Temperature (K)	120
a, *c* (Å)	18.5871 (5), 41.033 (2)
V (Å^3)	14176.0 (9)
Z	4
Radiation type	Cu *K*α
μ (mm^{-1})	0.62
Crystal size (mm)	0.20 × 0.20 × 0.02
Absorption correction	Gaussian
T_{min}, T_{max}	0.890, 0.991
No. of measured, independent and observed [$I > 2s(I)$] reflections	29384, 4030, 2982
R_{int}	0.081
$(\sin\theta/\lambda)_{max}$ (Å^{-1})	0.625
$R[F^2 > 2s(F^2)]$, $wR(F^2)$, *S*	0.056, 0.174, 1.07
No. of reflections	4030
No. of parameters	129
No. of restraints	2
H-atom treatment	H-atom parameters constrained
$D\rho_{max}$, $D\rho_{min}$ (e Å^{-3})	0.94, -0.69

Table S3. Crystal data and structure refinement details for MFM-182

Identification code	MFM-182
Chemical formula	($C_{66}H_{40}Cu_4O_{20}$)
M_r	1407.14
Crystal system, space group	Tetragonal, *I*4/*mmm*
Temperature (K)	120
a, *c* (Å)	18.5802 (4), 45.903 (3)
V (Å^3)	15847 (1)
Z	4
Radiation type	Cu *K*α
μ (mm^{-1})	0.85
Crystal size (mm)	0.19 × 0.18 × 0.02
Absorption correction	Gaussian
T_{min}, T_{max}	0.876, 0.981
No. of measured, independent and observed [I > 2s(I)] reflections	20867, 4459, 2938
R_{int}	0.055
(sin θ/ λ)$_{max}$ (Å^{-1})	0.625
$R[F^2 > 2s(F^2)]$, $wR(F^2)$, S	0.062, 0.205, 1.02
No. of reflections	4459
No. of parameters	135
No. of restraints	2
H-atom treatment	H-atom parameters constrained
Dρ$_{max}$, Dρ$_{min}$ (e Å^{-3})	0.35, −0.30

Table S4. Crystal data and structure refinement details for MFM-183

Identification code	MFM-183
Chemical formula	($C_{66}H_{38}Cu_4N_4O_{20}$)
M_r	3306.41
Crystal system, space group	Tetragonal, *I*4/*mmm*
Temperature (K)	120
a, *c* (Å)	18.6881 (3), 50.6437 (17)
V (Å^3)	17687.1 (7)
Z	4
Radiation type	Synchrotron, λ = 0.6889 Å
μ (mm^{-1})	0.52
Crystal size (mm)	0.2 × 0.2 × 0.02
Absorption correction	Multi-scan
T_{min}, T_{max}	0.774, 1.000
No. of measured, independent and observed [I > 2s(I)] reflections	115753, 8670, 4371
R_{int}	0.088
(sin θ/ λ)max (Å-1)	0.762
$R[F^2 > 2s(F^2)]$, $wR(F^2)$, S	0.083, 0.307, 1.09
No. of reflections	8670
No. of parameters	141
H-atom treatment	H-atom parameters constrained
Dρ$_{max}$, Dρ$_{min}$ (e Å^{-3})	0.51, -0.38

Table S5. Crystal data and structure refinement details for MFM-185

Identification code	MFM-185
Chemical formula	($C_{72}H_{40}Cu_4N_4O_{22}$)
M_r	3250.62
Crystal system, space group	Tetragonal, *I*4/*mmm*
Temperature (K)	293
a, *c* (Å)	18.476 (2), 59.999 (8)
V (Å^3)	20480 (4)
Z	4
Radiation type	Synchrotron, λ = 0.6889 Å
m (mm^{-1})	0.44
Crystal size (mm)	0.1 × 0.1 × 0.01
Absorption correction	Multi-scan
T_{min}, T_{max}	0.513, 1.000
No. of measured, independent and observed [I > 2s(I)] reflections	33932, 5441, 1852
R_{int}	0.132
(sin θ/ λ)$_{max}$ (Å^{-1})	0.610
$R[F^2 > 2s(F^2)]$, $wR(F^2)$, S	0.103, 0.400, 1.01
No. of reflections	5441
No. of parameters	153
H-atom treatment	H-atom parameters constrained
Dρ$_{max}$, Dρ$_{min}$ (e Å^{-3})	0.38, -0.43

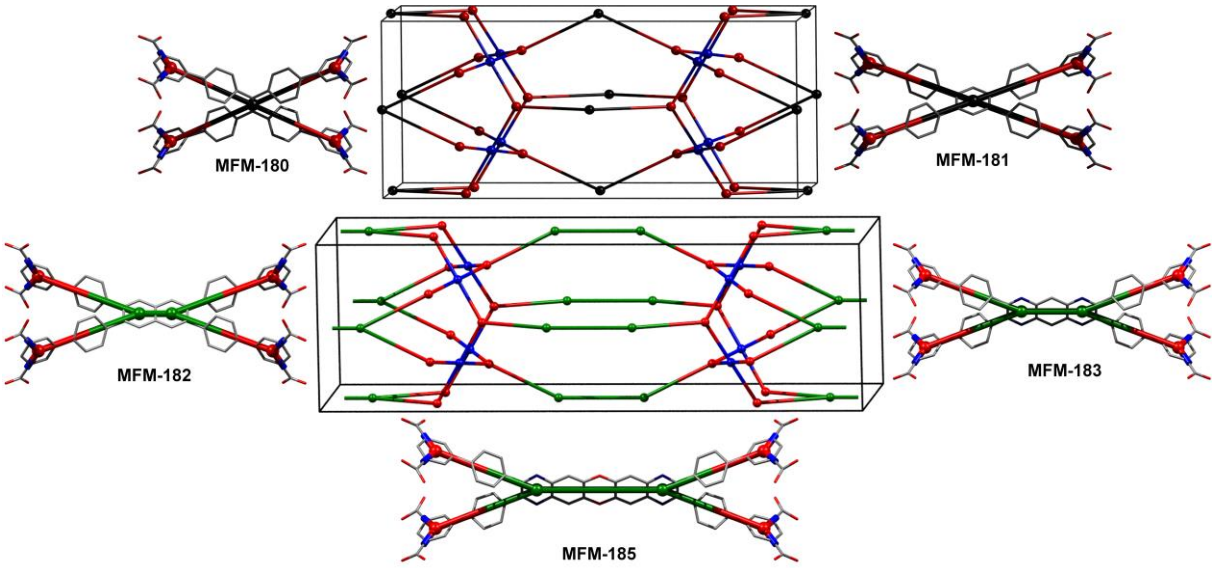

Figure S1. Topological simplification of the organic linkers and resulting **tbo** (top) and **3,3,4-c** (bottom) nets.

Powder X-ray diffraction (PXRD)

The phase purity of the bulk samples was confirmed by powder X-ray diffraction (Figure S4). Samples were activated, placed in a glovebox under Ar and then loaded into sample holders sealed with a polyimide (Kapton®) film. The PXRD measurements were carried out at room temperature on a PANalytical X'Pert PRO diffractometer using Cu-Kα radiation (λ = 1.5418 Å) at a scan speed of 0.02 °/s and a step size of 0.02 ° in 2θ.

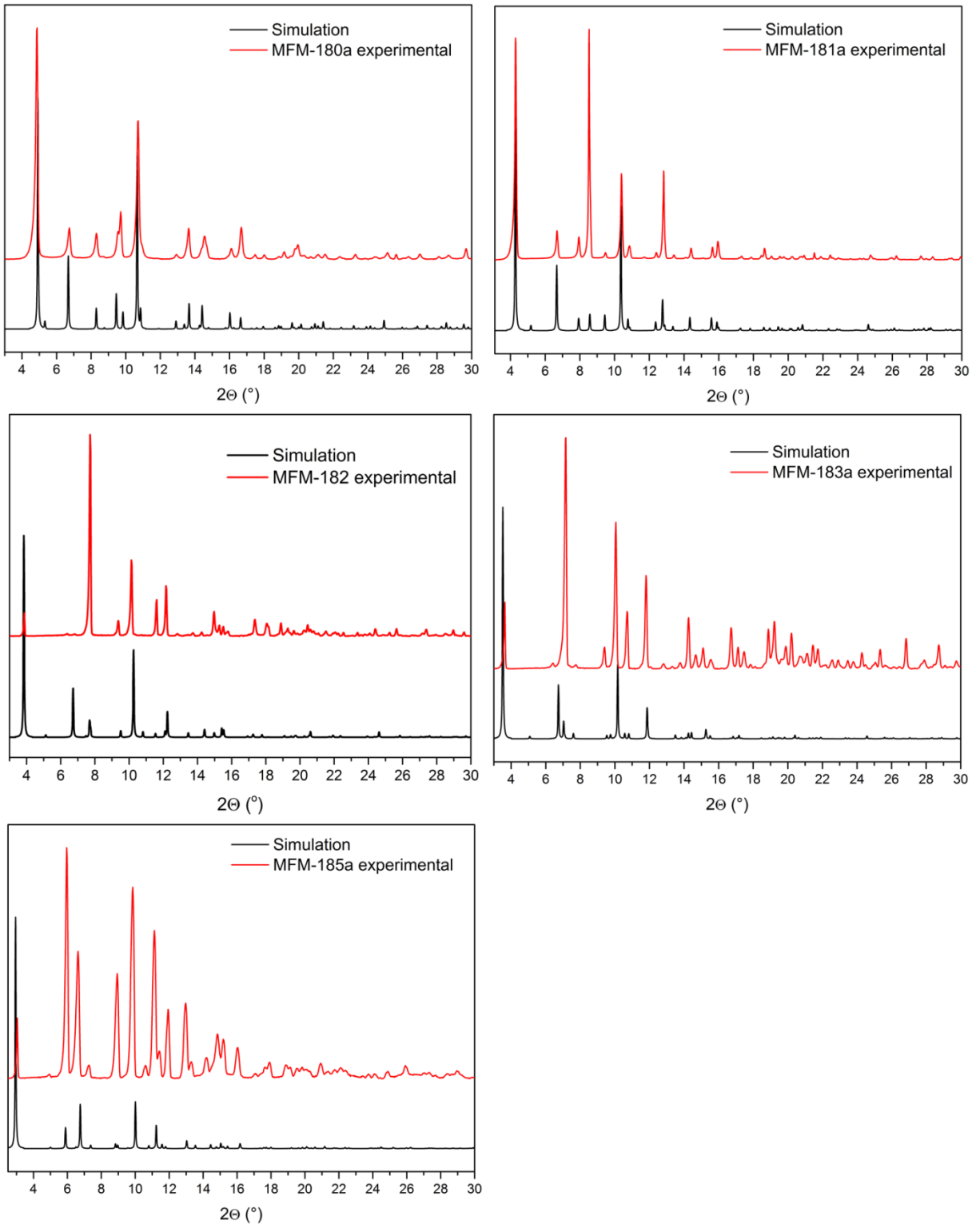

Figure S2. Experimental and simulated (from single crystal structures) PXRD patterns of MFM-180a, MFM-181a, MFM-182a, MFM-183a, and MFM-185a. The experimental patterns were collected under inert atmosphere using desolvated samples.

Thermogravimetric analysis

The as-synthesized frameworks MFM-180, -181, -183 and -185 show very similar thermal behaviour and stability, as determined by thermogravimetric analysis (Figure S3). An initial rapid mass loss is observed between room temperature and 90 °C corresponding to the loss of uncoordinated EtOH and H_2O molecules from the pores, followed by a more gradual evacuation of bound H_2O molecules and solvents (DEF, DMF and/or DMSO) with higher boiling points. The material is stable between 180 °C and 300 °C without weight loss, followed by the rapid decomposition of the organic linker at higher temperatures.

TGA was performed under a flow of air with a heating rate of 5 °C/min using a Perkin Elmer Pyris 1 thermogravimetric analyser.

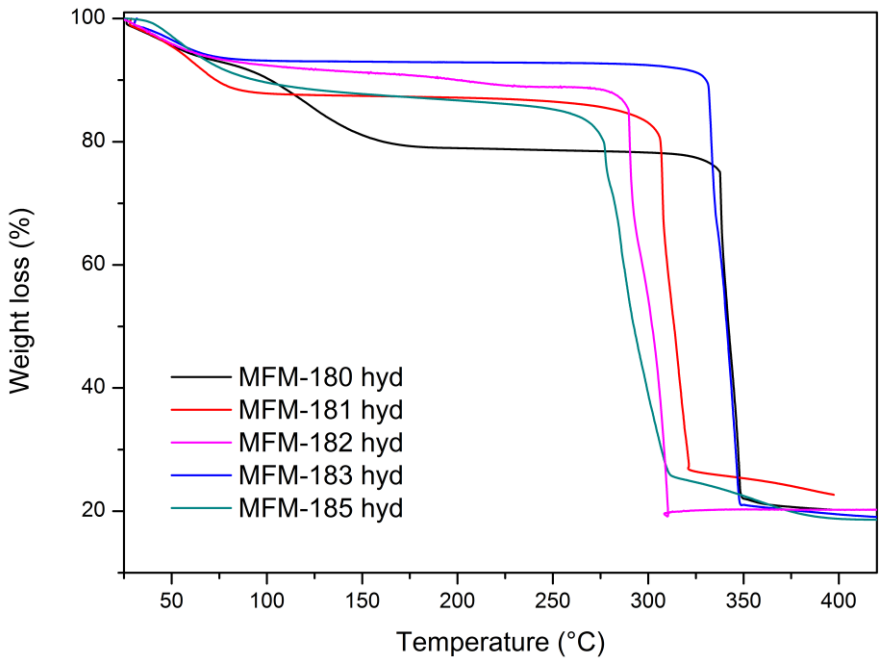

Figure S3. TGA plots of MFM-180, MFM-181, MFM-182, MFM-183 and MFM-185 after desolvation and exposure to ambient conditions.

MOF activation procedures

As-synthesised materials were solvent-exchanged with MeOH for 7 days. In the case of MFM-180 and MFM-181, the samples were then heated at 100 °C under dynamic vacuum for 16 h. In the case of MFM-183 and MFM-185, the MeOH exchanged samples were first activated *via* supercritical CO_2 drying using a Toumisis Autosamdri®-815, Series A critical point dryer, then transferred to a glovebox under Ar. The $ScCO_2$ dried samples were then transferred onto the gas adsorption instruments under inert atmosphere and heated at 100 °C under dynamic vacuum for 16 h.

N_2, H_2, CO_2 and CH_4 isotherms

Volumetric N_2, CO_2 and CH_4 isotherms for pressures in the range 0-1 bar were determined using a Quantachrome Instruments Autosorb-1. The data obtained was used for surface area and pore size distribution determination and for heat of adsorption calculations. For pressures in the range 0-20 bar, the H_2, CO_2 and CH_4 isotherms were measured on a Hiden Isochema intelligent gravimetric analyser (IGA). All data were corrected for the buoyancy of the system, samples and absorbates. Volumetric CH_4 sorption measurements were performed at General Motors over a pressure range of 0-60 bar using a HPVA-100 high-pressure analyzer (VTI Corporation). Sample tubes of a known weight were loaded with approximately 300 mg of sample under an argon atmosphere. All measurements were made with 99.9 % purity CH4, and 99.999 % purity He, the latter being used for dead volume measurements.

BET plots calculated from N2 adsorption isotherms at 77K

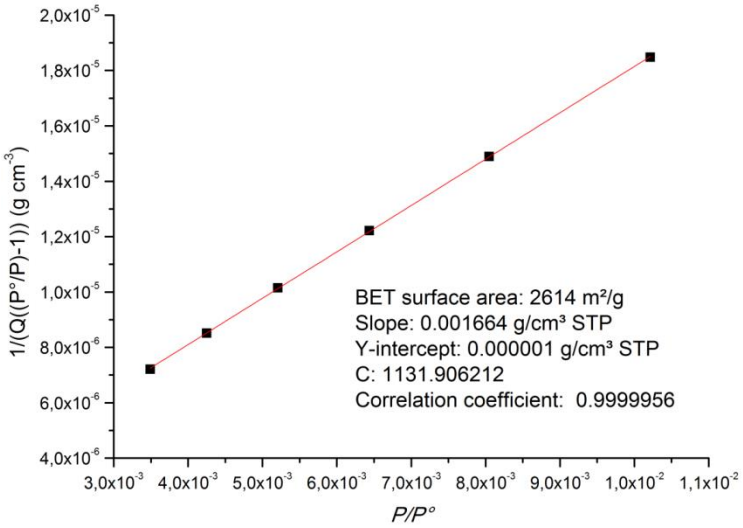

Figure S4. The BET plot derived from N_2 uptake in MFM-180a.

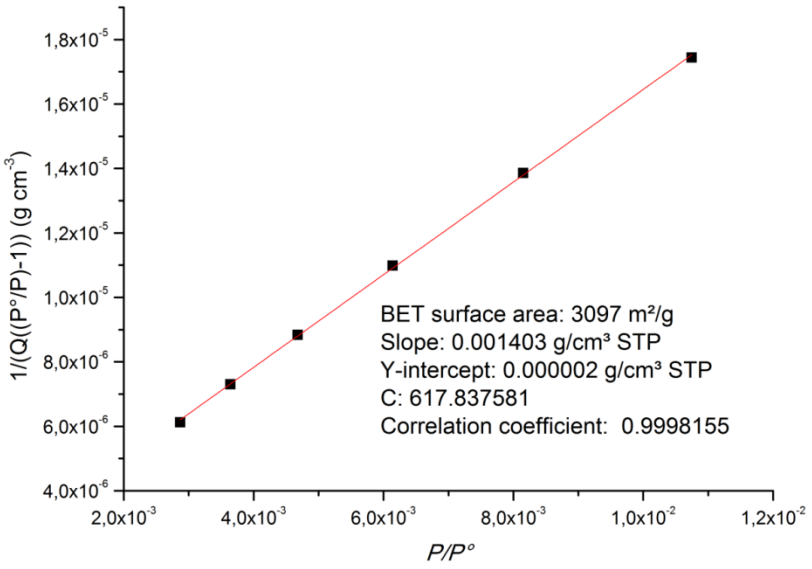

Figure S5. The BET plot derived from N_2 uptake in MFM-181a.

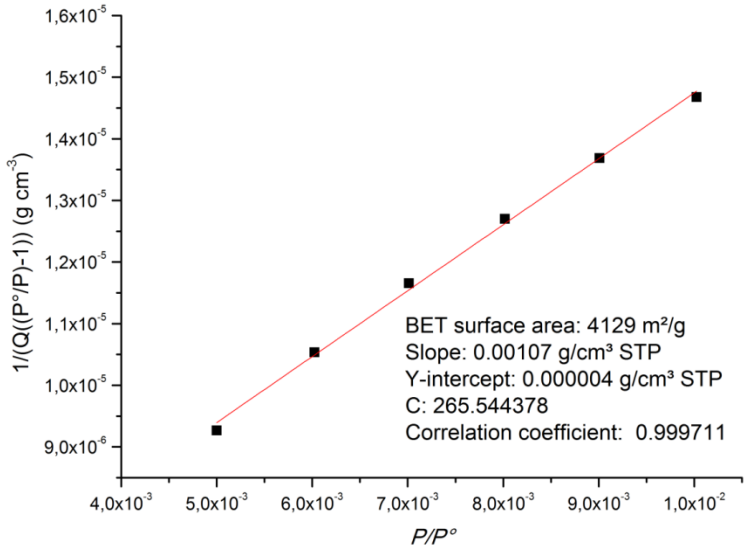

Figure S6. The BET plot derived from N_2 uptake in MFM-183a.

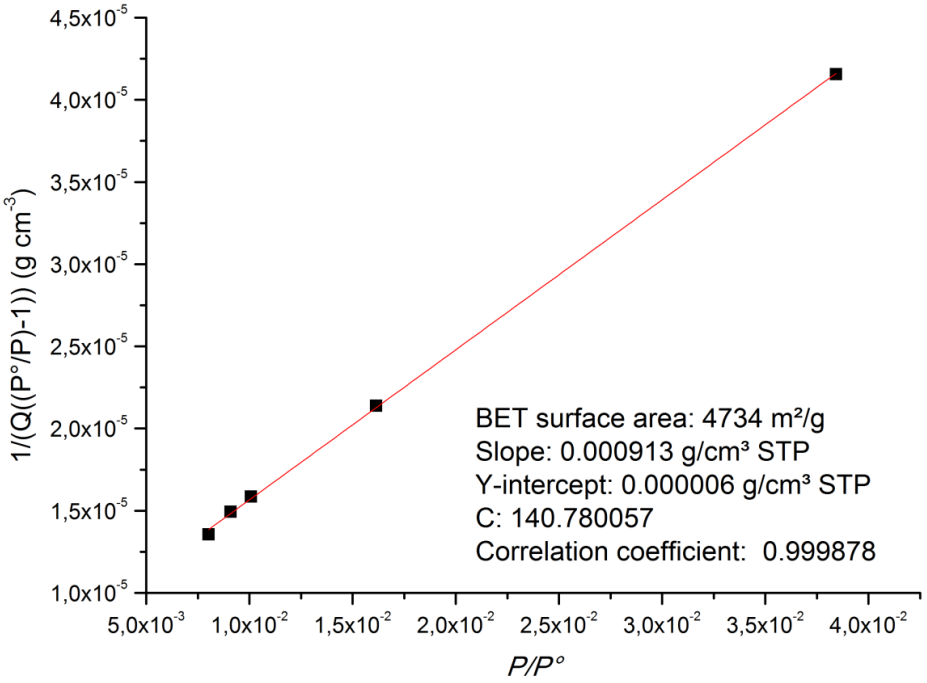

Figure S7. The BET plot derived from N_2 uptake in MFM-185a.

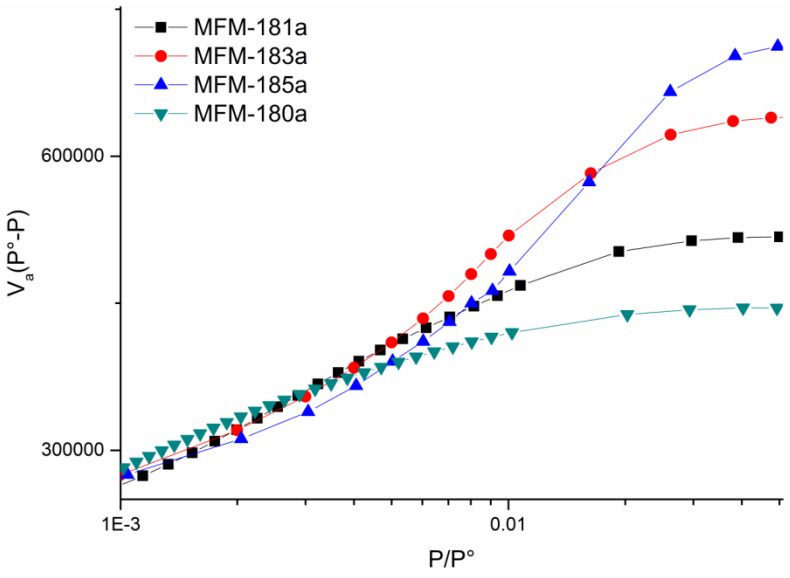

Figure S8. Consistency criterion[10] used to choose the P/P° range for the BET plots: Va(P° - P) plotted against P/P° for N_2, 77 K adsorption for framework materials.

***In Silico* Generation of MFM-184**

In lieu of successful synthesis of the H_8L^4 ligand targeted experimentally, the gas sorption properties of MFM-184 were calculated for a predicted crystal structure based on the assumption that the MOF is isoreticular to the other members of the MFM-18X series (Figure 3). The unit cell for MFM-184 was generated by first replacing the 5-fused heteroacene core of MFM-185 with a shorter, 4-fused core (Scheme 1) and reducing the length of the crystallographic *c*-axis to ensure appropriate connectivity within the structure. The cell parameters ($a = b = 18.4760$ Å, $c = 55.2550$ Å) and atomic coordinates were then optimised using the Forcite module implemented in Materials Studio, using the Universal Force Field[11] and charges calculated via the Electronegativity Equalization method.

BET plots calculated from simulated N_2 adsorption isotherms at 77K

The adsorption of N_2 at 77 K was simulated using the grand canonical Monte Carlo simulations implemented in the MuSiC software package[12] and using translation, rotation and energy-biased insertion and deletion moves. All simulations were allowed at least 8 x 106 equilibration steps, followed by 12 x 106 production steps for each pressure point. The frameworks were treated as rigid, with atoms kept fixed at their crystallographic positions. Lennard-Jones parameters for the framework atoms were taken from the OPLS[12] force field with the exception of copper, for which UFF parameters[14] were used. Nitrogen was simulated as a rigid molecule using the TraPPE model,[15] incorporating both Lennard-Jones parameters and partial charges. Previous work has shown that nitrogen-MOF electrostatic contributions play only a minor role in nitrogen adsorption[16] and, as such, only the electrostatic interactions between nitrogen molecules were included in our simulations.

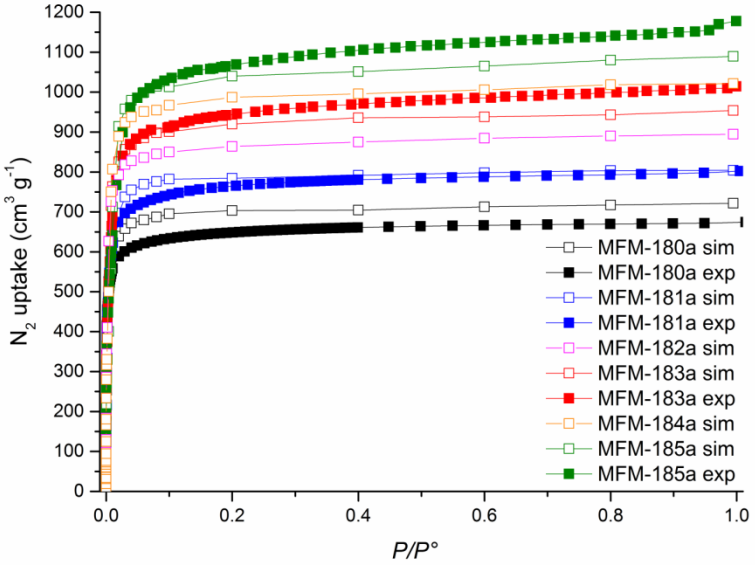

Figure S9. Simulated and experimental N_2 sorption isotherms for MFM-180a, -181a, -182a -183a, -184a and -185a at 77 K.

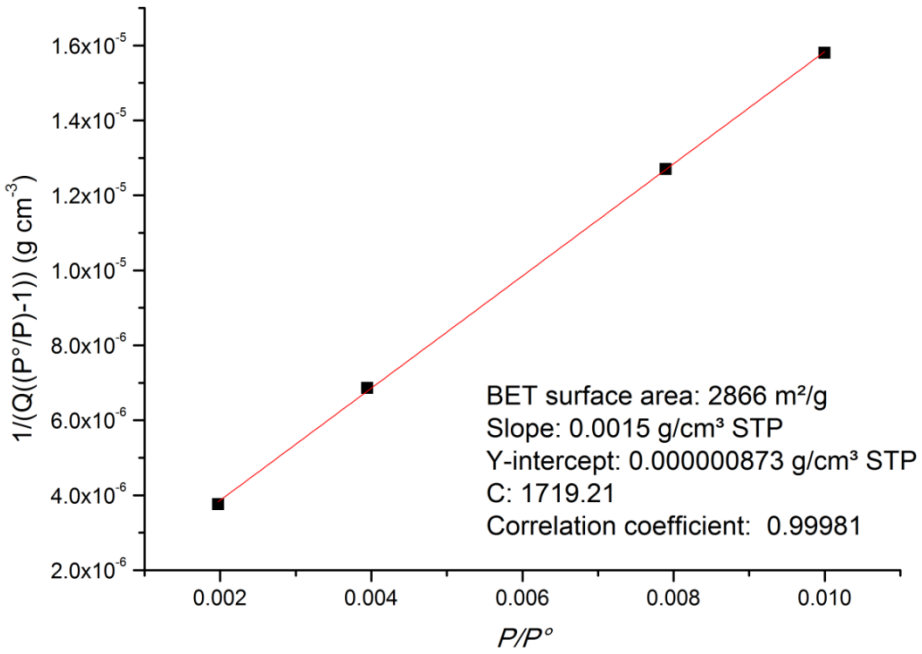

Figure S10. The BET plot derived from simulated N_2 uptake in MFM-180a.

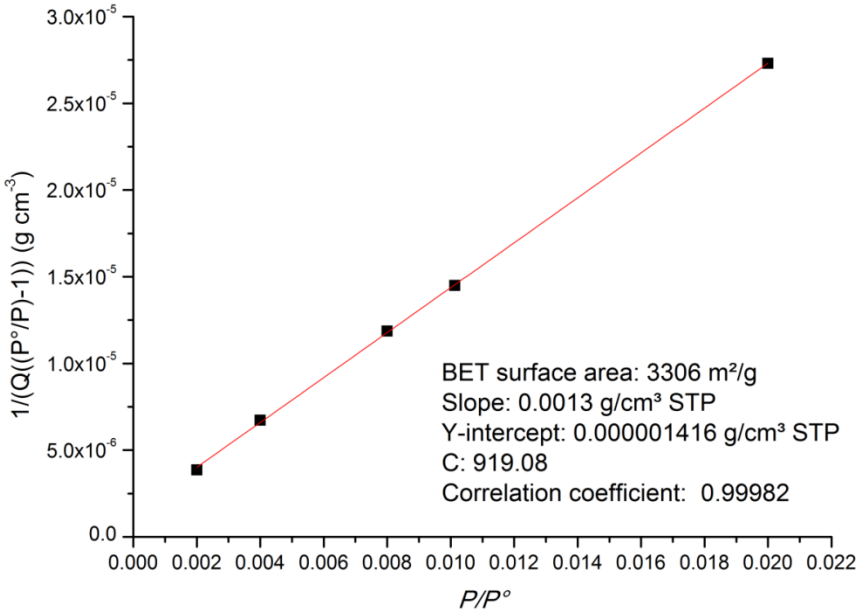

Figure S11. The BET plot derived from simulated N_2 uptake in MFM-181a.

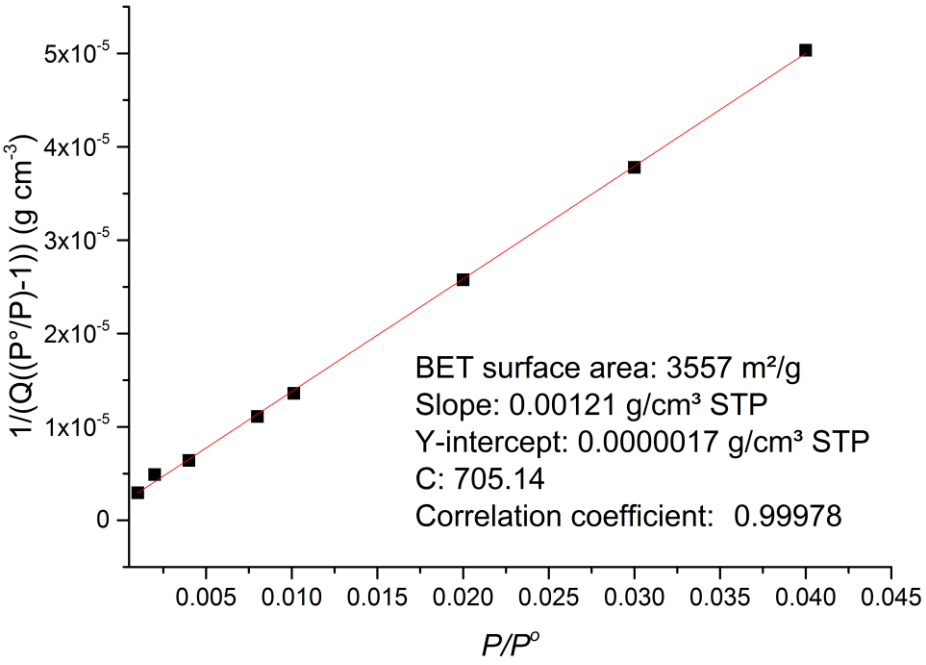

Figure S12. The BET plot derived from simulated N_2 uptake in MFM-182a.

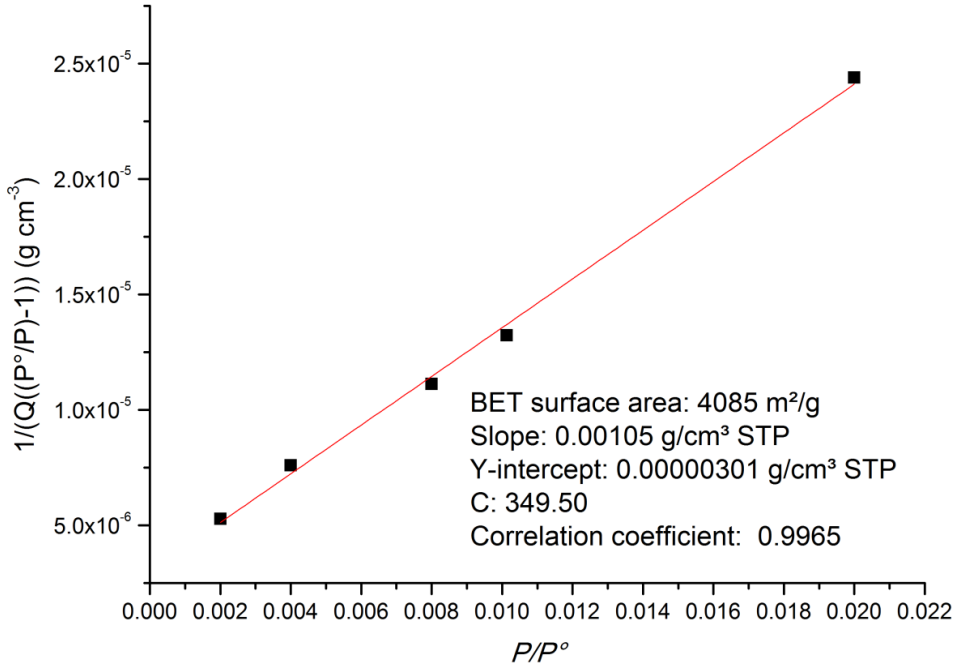

Figure S13. The BET plot derived from simulated N_2 uptake in MFM-183a.

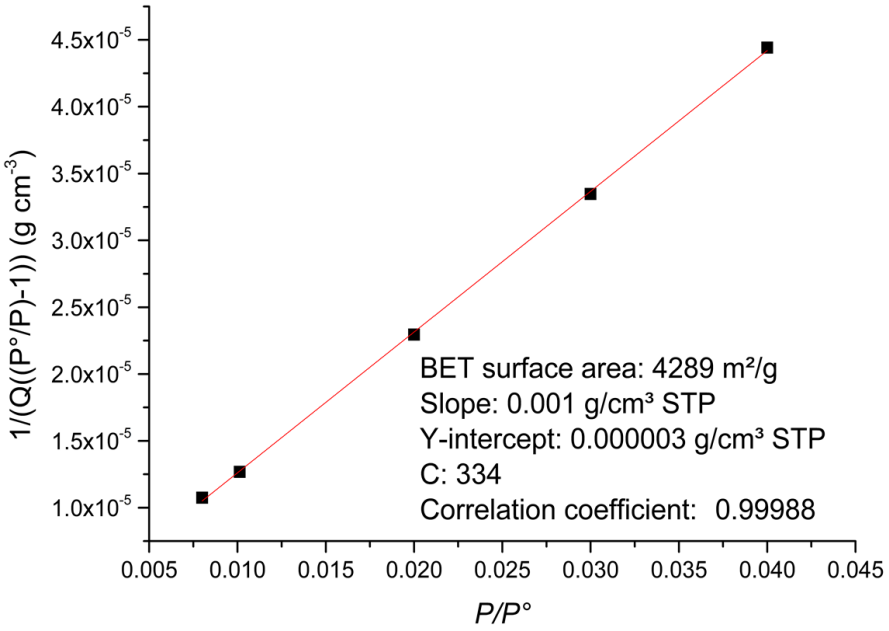

Figure S14. The BET plot derived from simulated N_2 uptake in MFM-184a.

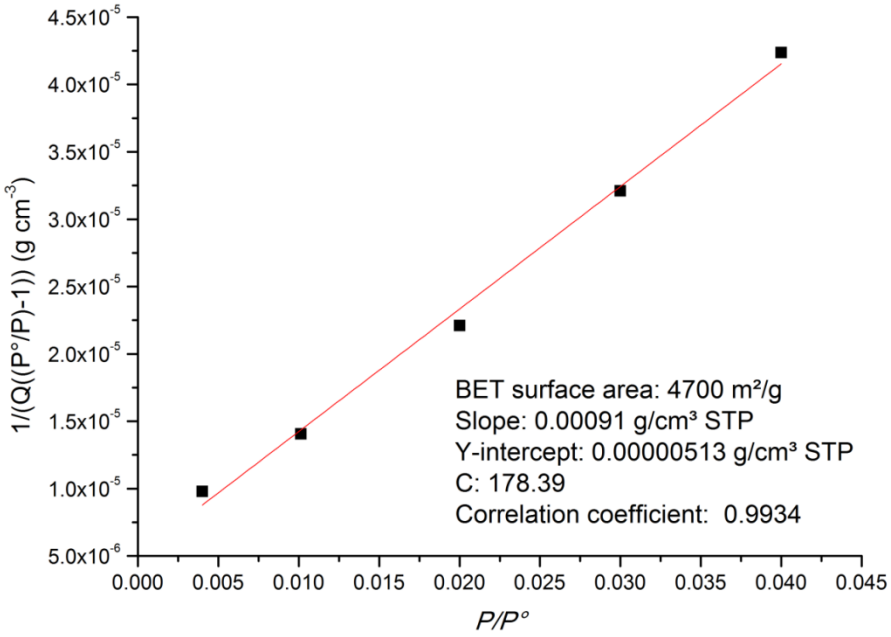

Figure S15. The BET plot derived from simulated N_2 uptake in MFM-185

Heats of adsorption for CO_2 and CH_4 in MFM-18X frameworks

The CO_2 and CH_4 adsorption isotherms at 273 and 298 K were fitted to the virial equation (eq 3, virial method I):[17]

$$\ln(n/P) = A_0 + A_1 * n + A_2 * n^2 + A_3 * n^3 + \ldots \quad (1)$$

where P is the pressure, n is total amount adsorbed and A_0, A_1, A_2, etc. are virial coefficients. The Henry's Law constant is given by $K_H = \exp(A_0)$. The enthalpy of adsorption at zero coverage was determined from the relationship:

$$\delta A_0 = R Q_{st}^{n=0} \delta(T^{-1}) \quad (2)$$

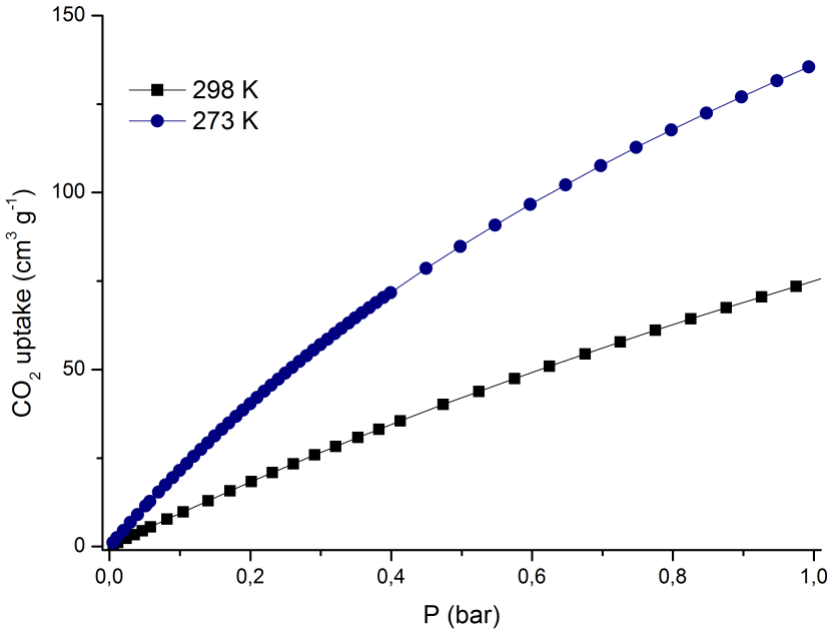

Figure S16. CO_2 sorption isotherms for MFM-180a at 273 and 298 K.

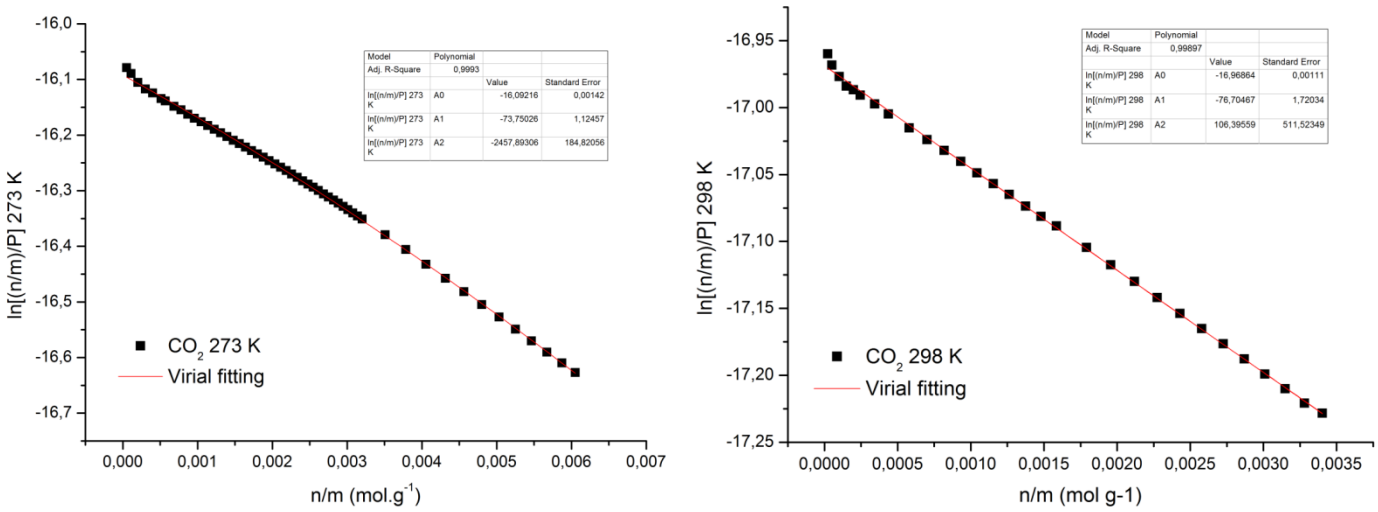

Figure S17. Virial analysis of the CO2 isotherms for MFM-180a at 298 and 273 K.

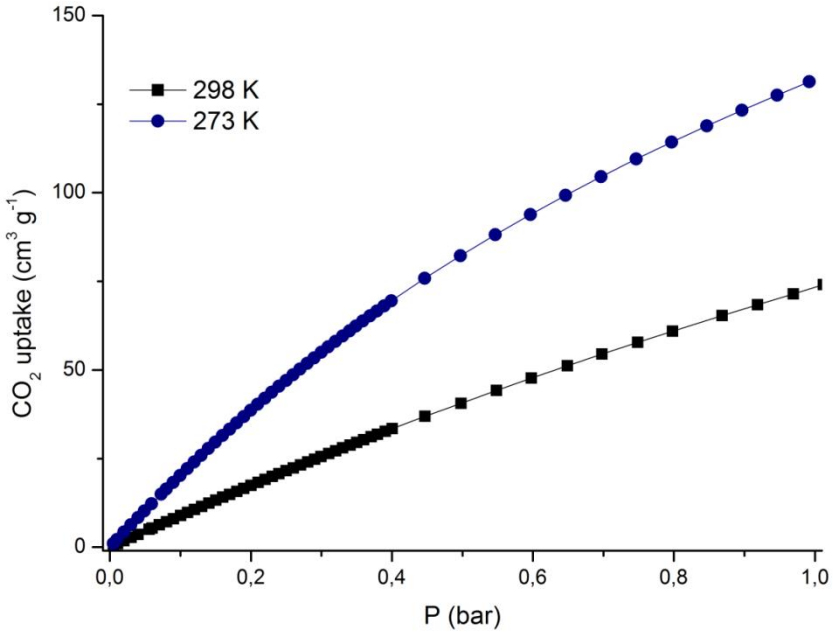

Figure S18. CO_2 sorption isotherms for MFM-181a at 273 and 298 K.

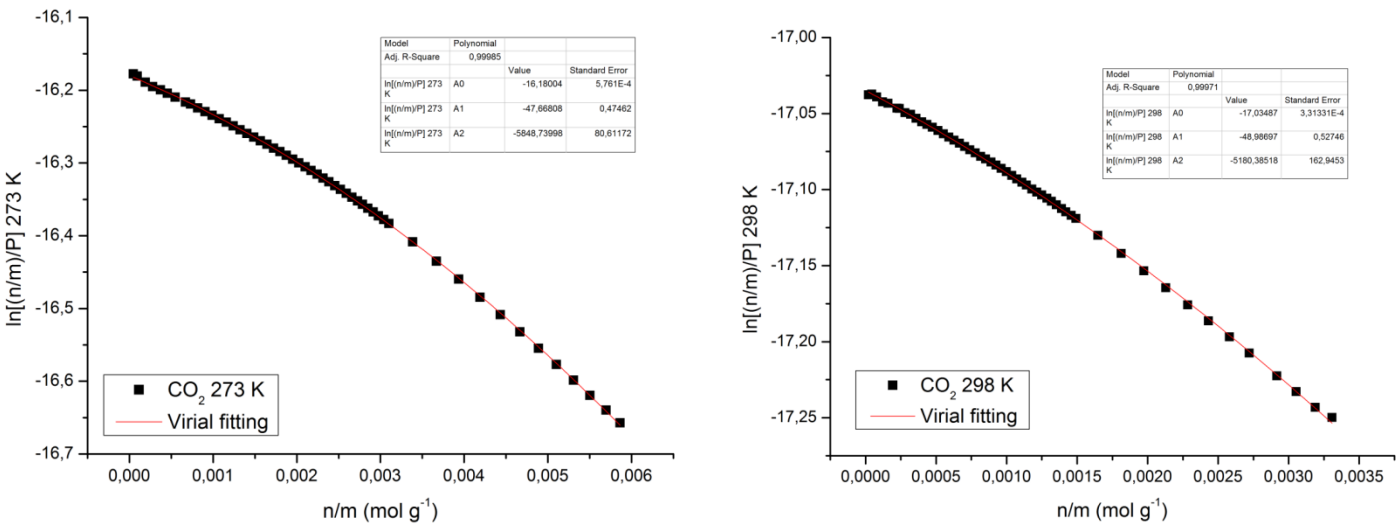

Figure S19. Virial analysis of the CO_2 isotherms for MFM-181a at 298 and 273 K

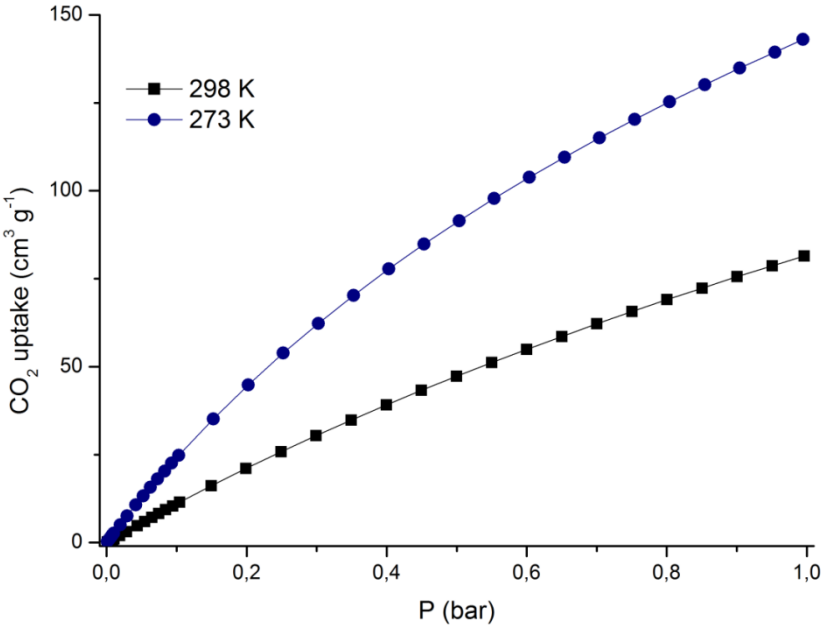

Figure S20. CO_2 sorption isotherms for MFM-183a at 273 and 298 K.

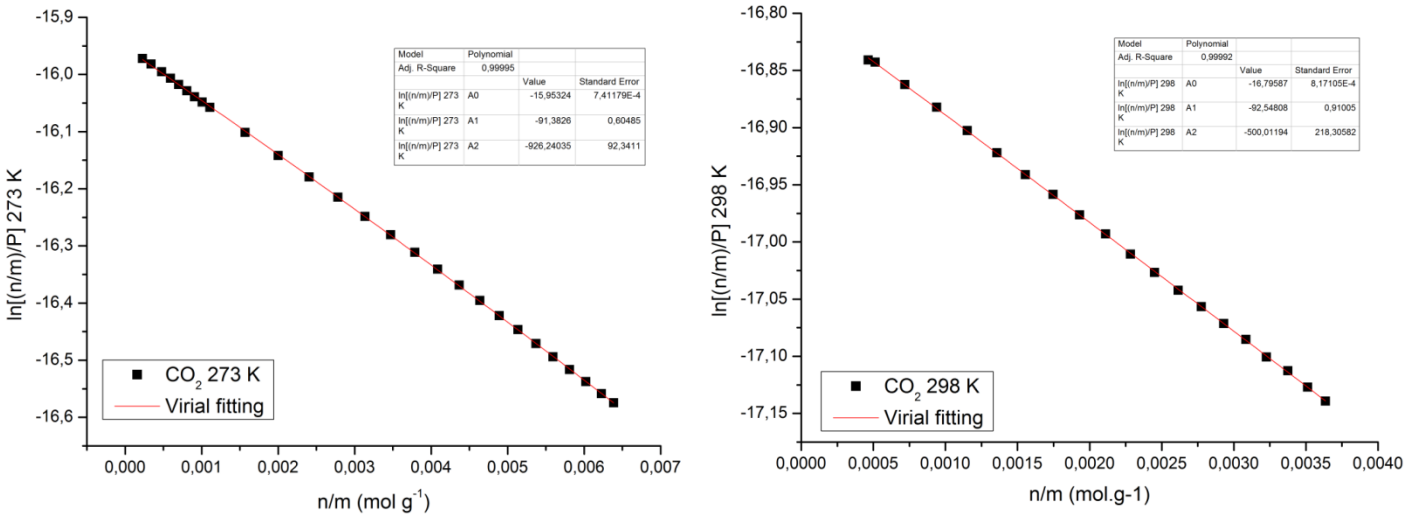

Figure S21. Virial analysis of the CO_2 isotherms for MFM-183a at 298 and 273 K

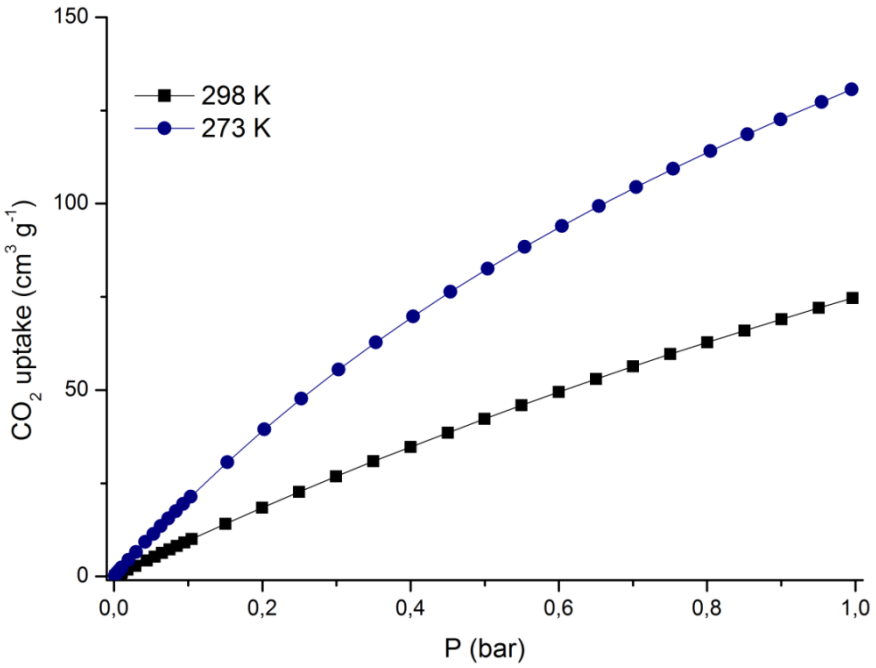

Figure S22. CO_2 sorption isotherms for MFM-185a at 273 and 298 K.

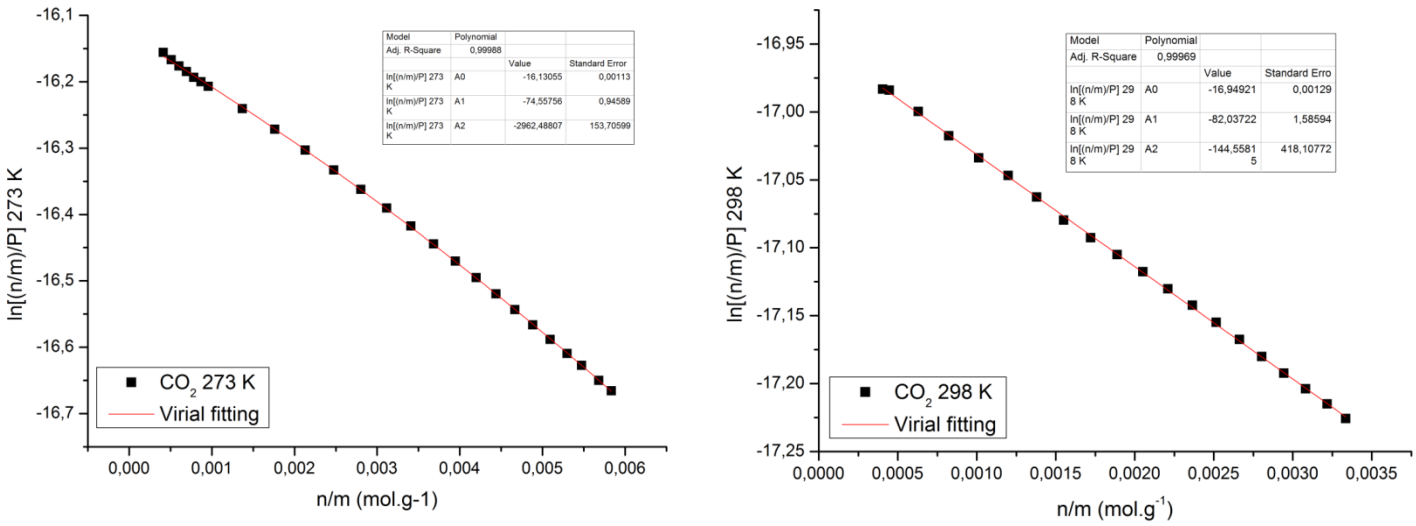

Figure S23. Virial analysis of the CO_2 isotherms for MFM-185a at 298 and 273 K

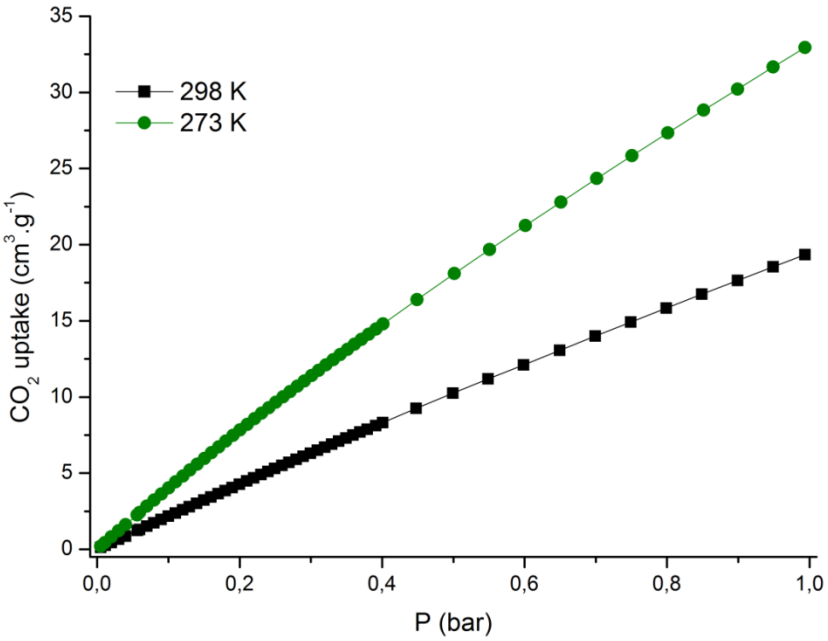

Figure S24. CH_4 sorption isotherms for MFM-180a at 273 and 298 K.

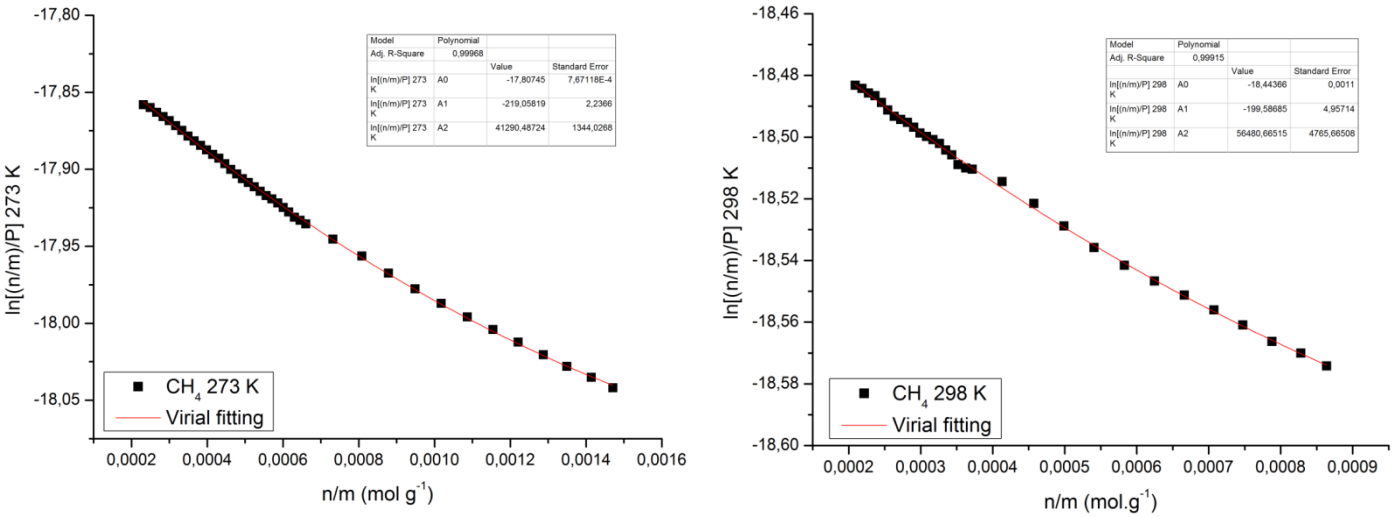

Figure S25. Virial analysis of the CH_4 isotherms for MFM-180a at 298 and 273 K

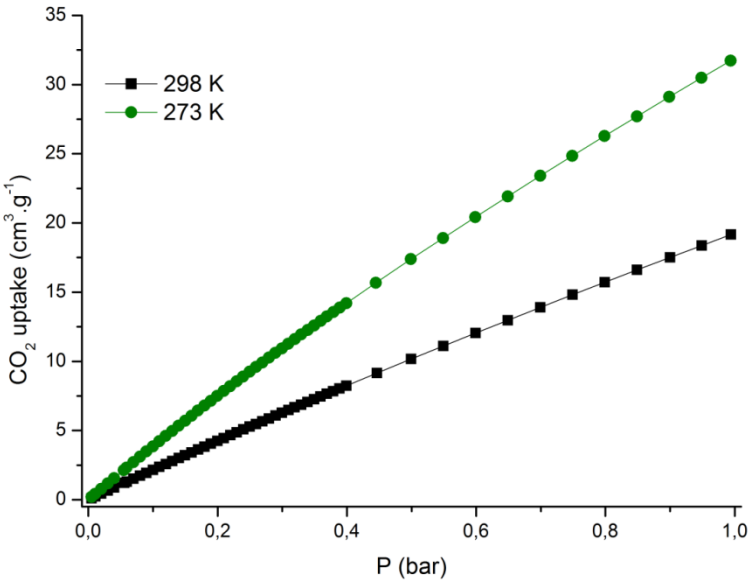

Figure S26. CH_4 sorption isotherms for MFM-181a at 273 and 298 K.

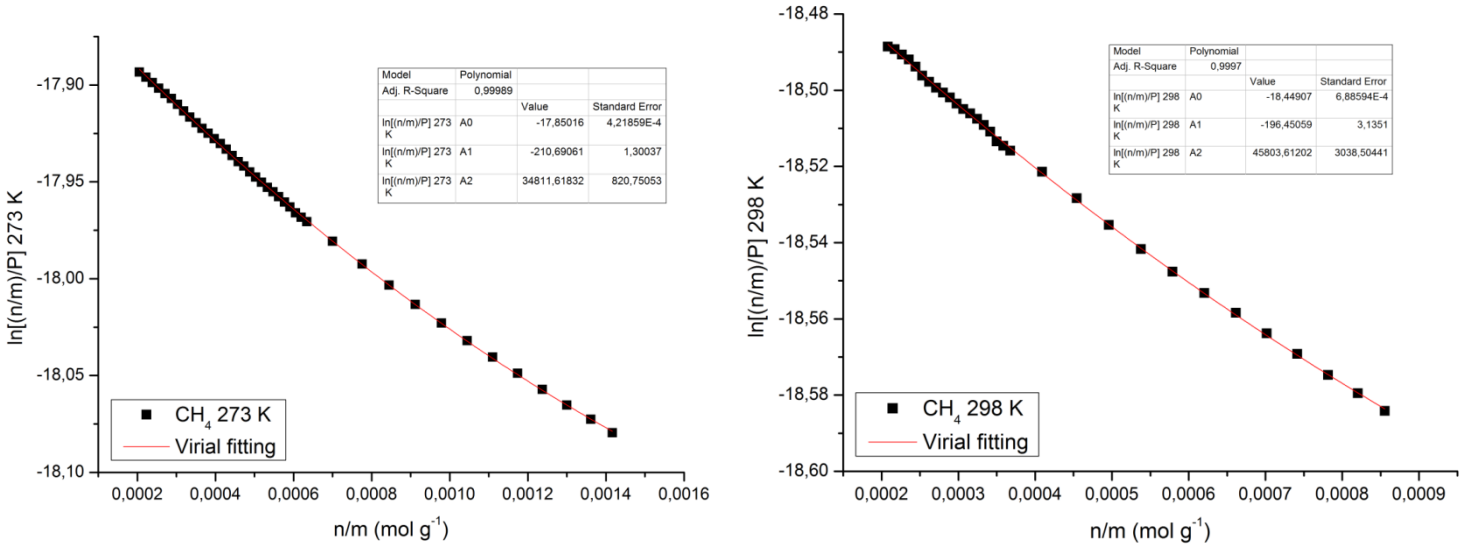

Figure S27. Virial analysis of the CH_4 isotherms for MFM-181a at 298 and 273 K

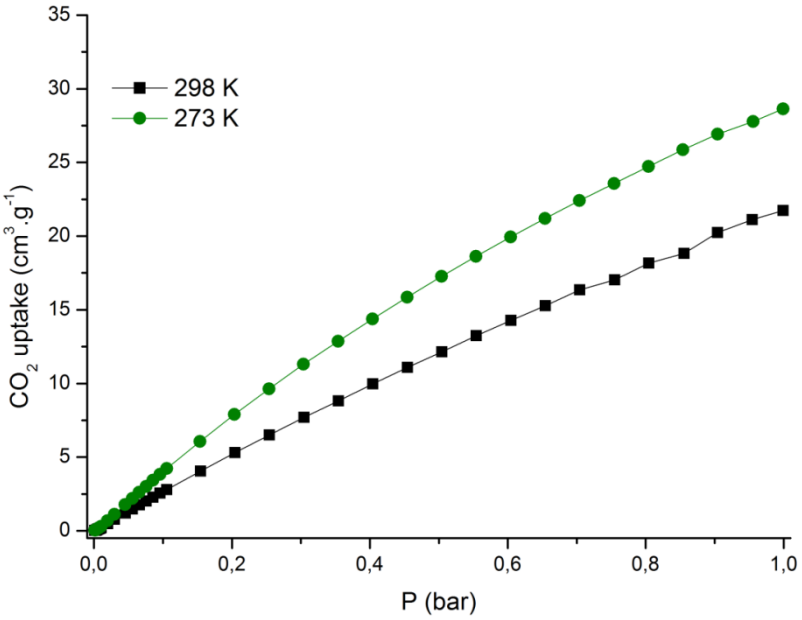

Figure S28. CH_4 sorption isotherms for MFM-183a at 273 and 298 K.

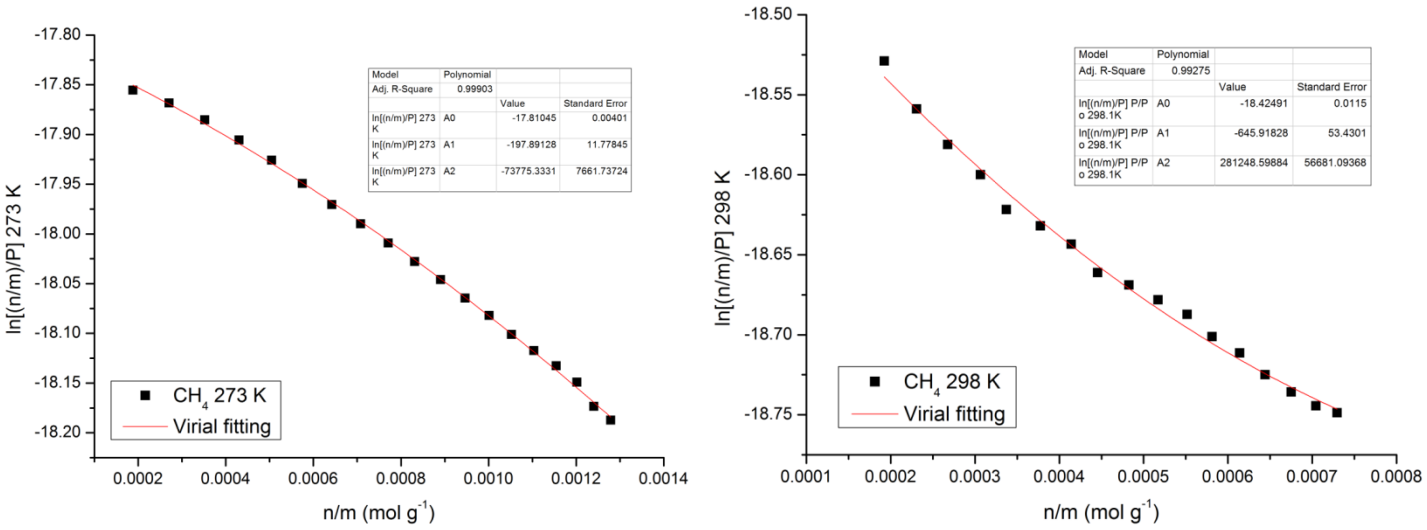

Figure S29. Virial analysis of the CH_4 isotherms for MFM-183a at 298 and 273 K

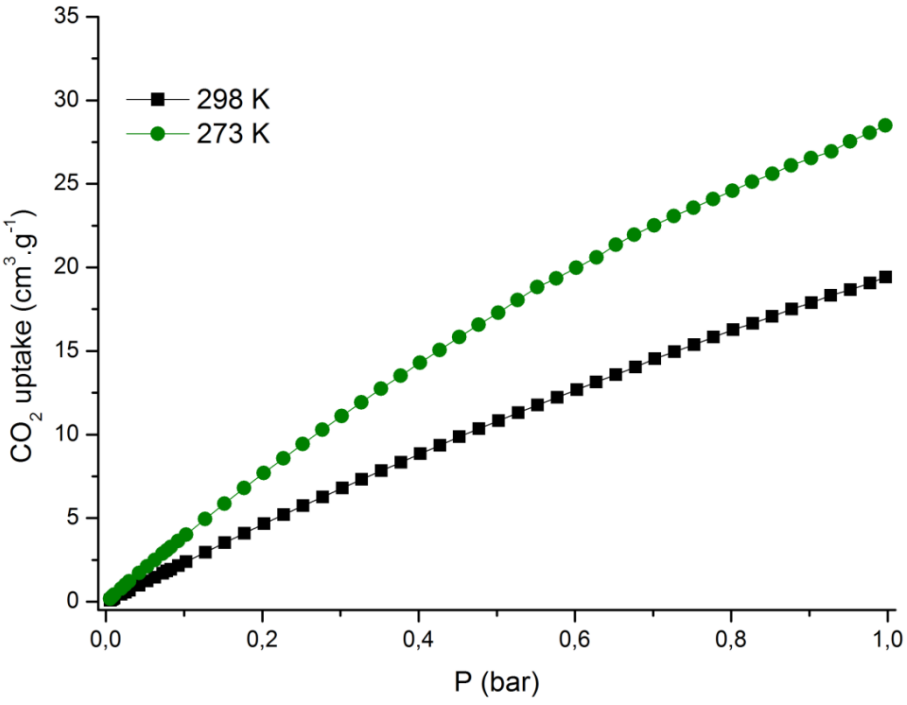

Figure S30. CH_4 sorption isotherms for MFM-185a at 273 and 298 K.

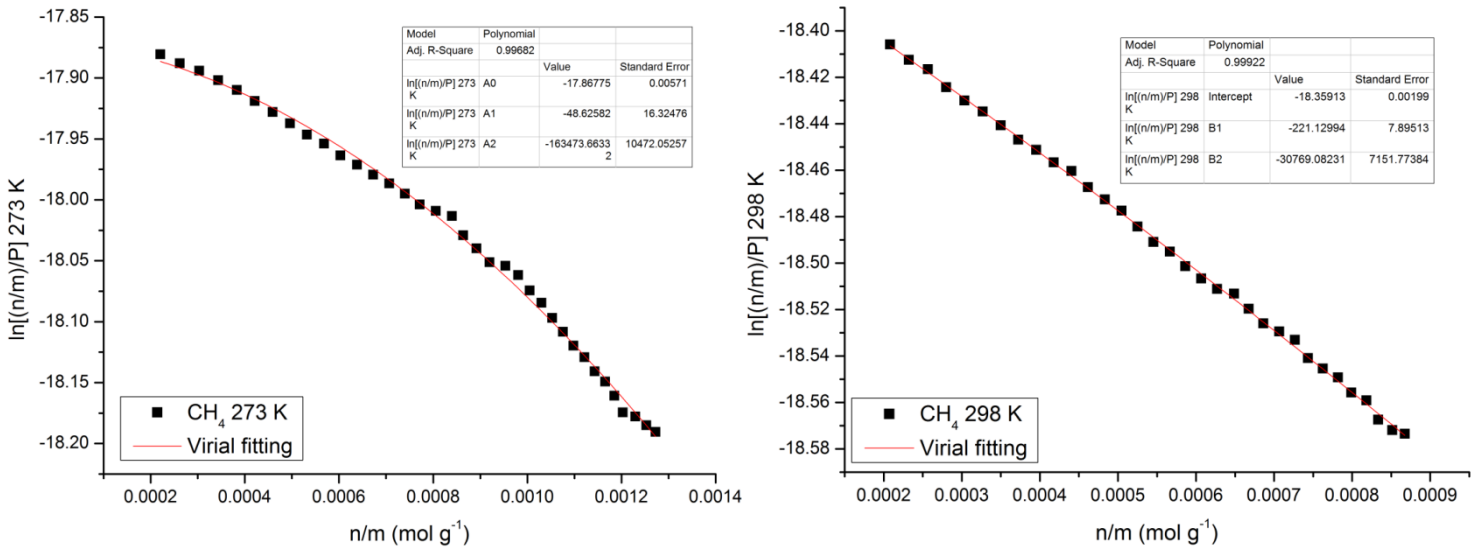

Figure S31. Virial analysis of the CH_4 isotherms for MFM-185a at 298 and 273 K

Table S6. Comparison of CH_4 adsorption properties for selected octacarboxylate $[Cu_2(O_2CR)_4]$ paddlewheel MOFs.

	CH_4 uptake [a] [g g^{-1}]	CH_4 uptake[a] [cm^3 cm^{-3} STP]	CH_4 uptake[b] [g g^{-1}]	CH_4 uptake[b] [cm^3 cm^{-3} STP]	Working capacity[c] [g g^{-1}]	Working capacity[c] [cm^3 cm^{-3}]
MFM-181	0.189	159	0.212	179	0.157	132
MFM-183	0.191	143	0.262	197	0.209	157
MFM-185	0.204	138	0.290	197	0.240	163
PCN-80[30]	0.177	142	-	-	-	-
Cu-tbo-MOF-5[31]	0.170	151	0.238	199	0.189	158

[a] 35 bar, 298 K; [b] 298 K, 65 bar; [c] 5-65 bar

Table S7. Comparison of CO_2 adsorption properties for selected octacarboxylate$[Cu_2(O_2CR)_4]$ paddlewheel MOFs.

	1 bar (298 K)		20 bar (298 K)		
	wt %	cm^3 cm^{-3} (STP)	wt %	cm^3 cm^{-3} (STP)	Q_{st} (kJ.mol^{-1})
MFM-180	15.0	49.8	83.1	276.5	23.7
MFM-181	14.6	44.6	95.4	292.4	23.1
MFM-183	13.7	37.2	96.7	263.3	22.9
MFM-185	13.0	32.2	107.3	265.0	22.7
PCN-80[30]	12.0	35.1	72.8	213.2	-
NOTT-140[23]	-	-	91.2[a]	314.2[a]	24.7

[a] 293 K

Solid state ^{2}H NMR spectroscopy of deuterated MFM-180 and MFM-181 frameworks

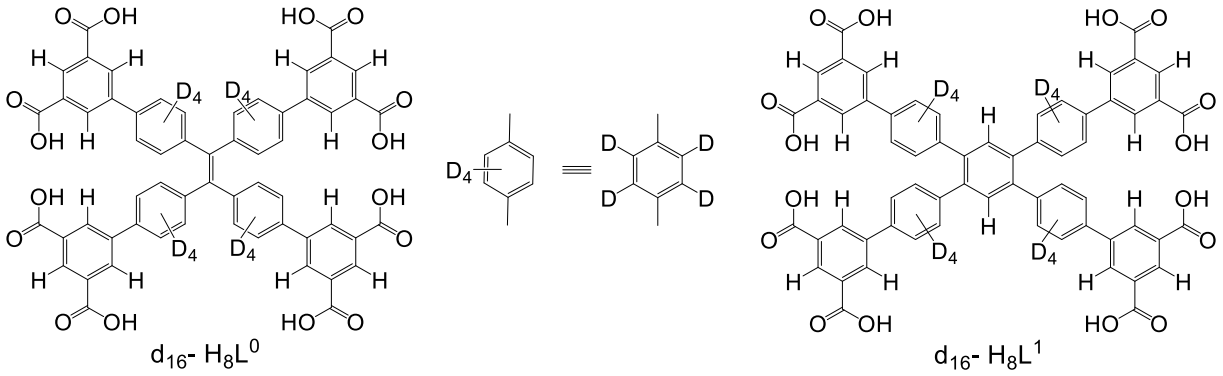

Scheme S2. The selectively deuterated linkers H_8L^0-d_{16} and H_8L^1-d_{16} used for the synthesis of deuterated MFM-180-d_{16} and MFM-181-d_{16}.

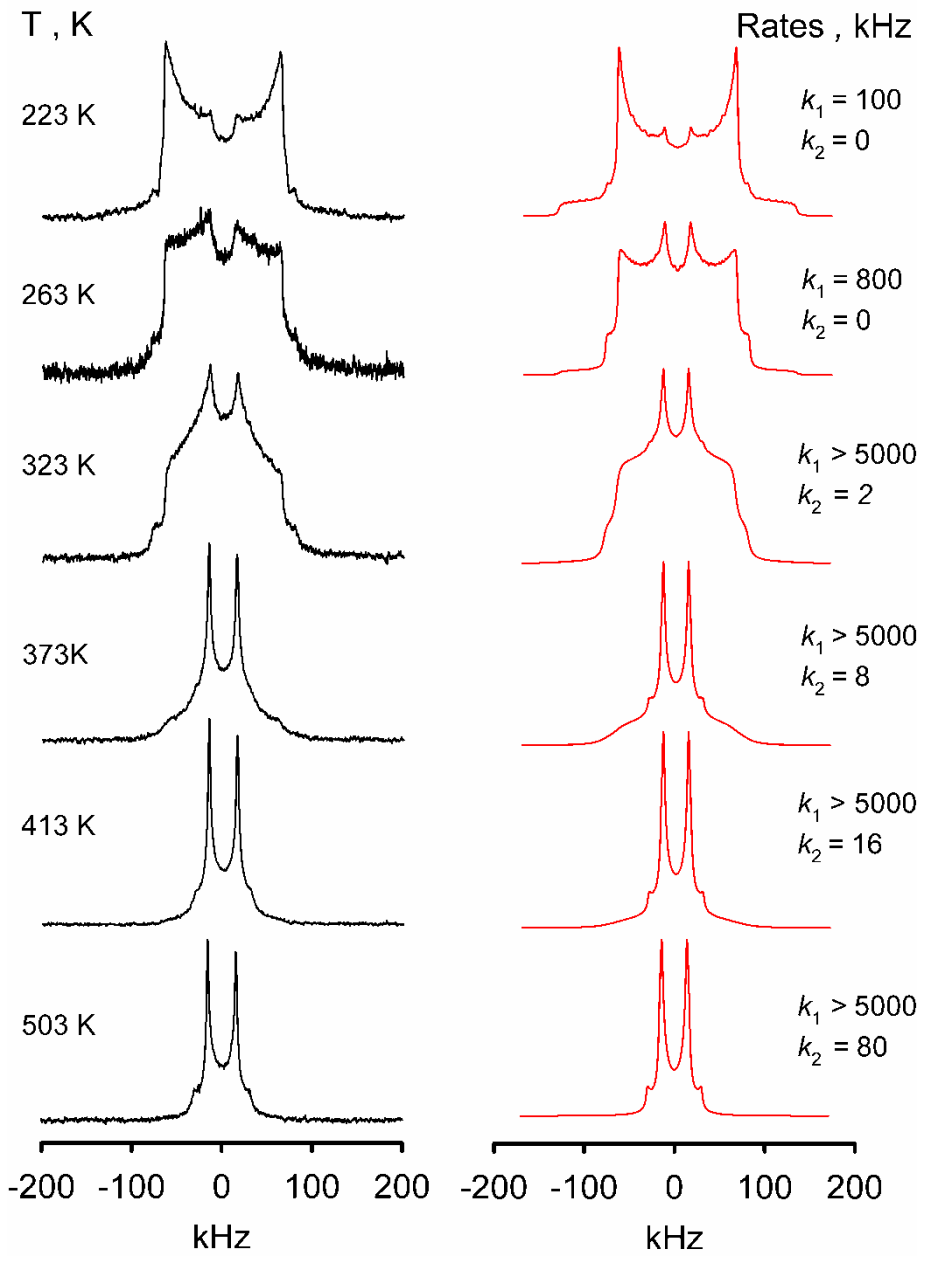

Figure S32. Temperature dependence of the ^{2}H NMR spectral line shape for the phenyl fragments in MFM-180-d_{16} (experimental - black, simulation - red). 2-Site exchange patterns were observed for T < 323 K requiring the introduction of a distribution of flipping rate constants; we assumed a log-normal distribution with a distribution width **σ** ~ 1. The line-width was taken to be **dω** = 0.5 kHz.

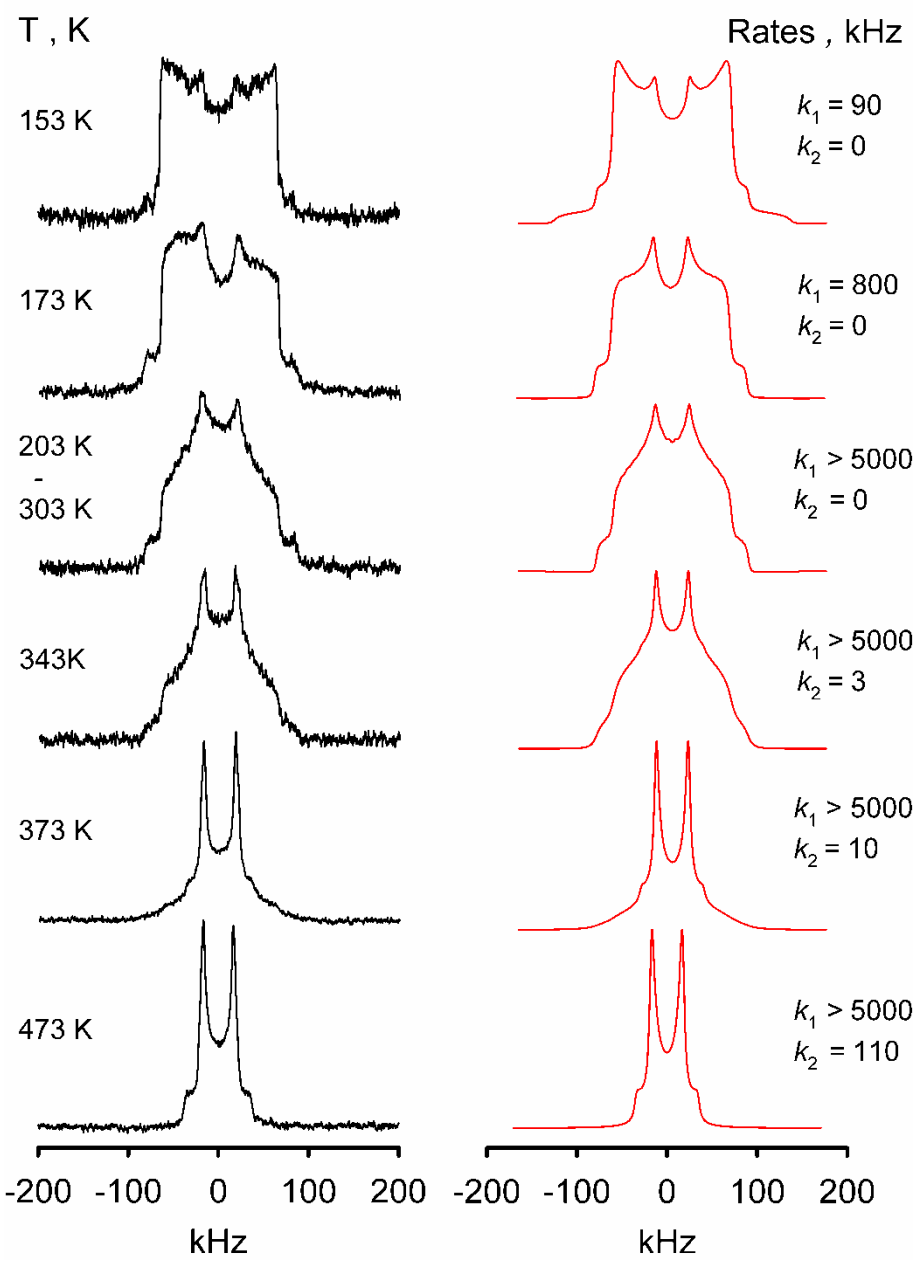

Figure S33. Temperature dependence of the ^{2}H NMR spectral line shape for the phenyl fragments in MFM-181-d_{16} (experimental - black, simulation - red). 2-Site exchange patterns were observed for T < 343 K requiring the introduction of a distribution of flipping rate constants; we assumed a log-normal distribution with a distribution width $\boldsymbol{\sigma}$ ~ 2. The line-width was taken to be $\mathbf{d\omega}$ = 2 kHz.

^{2}H NMR spectra line shape simulation.

To understand the detailed mechanism of rotations and their kinetic parameters (the activations barriers and rate constants), a detailed fitting analysis of the ^{2}H NMR spectral line shape across a temperature range was performed. The FORTRAN simulation routines used are based on the general formalism proposed by Abragam[18] and developed in detail by Spiess[19] and others.[20–23] The fitted spectra were obtained by Fourier transform of the powder-average over the polar angles θ and φ of the correlation function $G(t,\theta,\varphi)$, which governs the time evolution of the transverse ^{2}H spin magnetization after the solid echo pulse sequence. The correlation function can be computed using the following equation:[21]

$$G(t,\theta,\varphi) = \sum_{i,j,k}^{1..N} \mathbf{l}_i \left[\exp(\mathbf{A}t)\right]_{ij} \left[\exp(\mathbf{A}\tau)\right]_{ij} \left[\exp(\mathbf{A}*\tau)\right]_{jk} \mathbf{P}_k \,, \tag{1}$$

where **A** is a complex matrix composed as follows:

$$\mathbf{A} = \Omega + \mathrm{K}\,, \tag{2}$$

The diagonal matrix Ω is composed by elements ω_i describing the frequencies of the exchanging sites, and K corresponds to a kinetic matrix that defines the jump rates.

$$\begin{cases} \Omega_{ii} = i\omega_i - 1/T_2^{\,0} \\ \Omega_{ij} = 0 \end{cases} \quad \text{and} \quad \begin{cases} \mathrm{K}_{ii} = -\sum_{j\neq i} k_{ij} \\ \mathrm{K}_{ij} = k_{ij} \end{cases}, \tag{3}$$

The $1/T_2^{\,0}$ term is the residual line width which reflects the contributions from homo- and heteronuclear dipolar interactions of the spin Hamiltonian. **l** is a vector (1,1,…,1) with N elements, where N is the number of exchange sites. **P** is a vector of equilibrium population of each site $p_{eq}(i)$. k_{ij} is the exchange rate between sites i and j. The ^{2}H NMR frequency at the i-th site $\omega_i(\theta,\varphi)$ is defined as:

$$\begin{aligned} \omega_i(\theta,\varphi) &= \sqrt{\frac{3}{2}}\frac{1}{2}\sum_{a,b=-2}^{2} q_{2a} D_{ba}(\Omega^i) D_{a0}(\varphi,\theta,0) \\ q_2 &= \left(-\frac{\eta}{2}, 0, \sqrt{\frac{3}{2}}, 0, -\frac{\eta}{2}\right) Q \end{aligned} \tag{4}$$

Here $D_{ba}(\Omega)$ are the Wigner rotation matrices[19] defining the C-D bond orientation for each site and q_2 is the static quadrupolar coupling tensor, with the Wigner matrices as defined by Spiess.[19] The q_2 tensor of a given deuteron is defined in the principle axis system (PAS), *i.e.*, a frame with the Z axis aligned with regard to C-D bond orientation. If the motion is complex, then the Winger matrix responsible for the transformation of the C-D bond orientation from the PAS (n = 1) frame to the frame attached to the molecular axis system (or the crystalline axis system, n=N) is a result of action of multiple Wigner matrices, each responsible for a certain rotation, *i.e.*,

$$D_{ba}(\Omega^i) = \sum_{c,d=-2}^{2} D_{bc}(\Omega^1) D_{cd}(\Omega^{\cdots}) D_{da}(\Omega^N) \tag{5}$$

In other words, to apply such jump-model concept to the particular case of the dynamics of the phenyl ring, a certain mechanism for these rotations has to be specified: a set of rotational matrices and the rate matrix that defines the exchange mechanism. Below is a typical and illustrative example of a 180° 2-site exchange case:

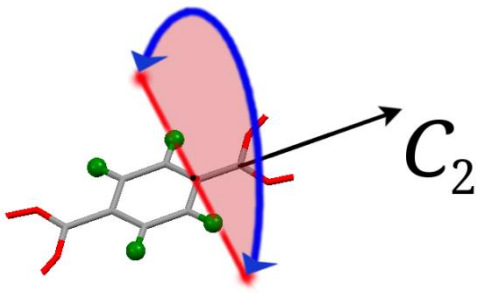

Figure S34: A phenyl ring exhibiting a large-amplitude 180° flips around the C_2 symmetry axis.

The 180° flips about the C_2 axis can be described by a 2x2 rate exchange matrix K:

$$K = \begin{bmatrix} -k_1 & k_1 \\ k_1 & -k_1 \end{bmatrix} \tag{6}$$

In the case when one of the motional process is characterized by a broad distribution of correlation times, the simulation procedure must be modified to take this into account. Physical reasons for such distribution are associated with samples inhomogeneity, either present due to the defects of the crystal structure, either induced by guests or other physical stimuli.

In our case, the flipping rate $k_f = k_1$ is characterized by a distribution. Since this distribution is broad and almost static over a broad temperature region, it can be assumed that the physical reason behind this is the variation in the torsional potential from one site to another. These variations are assumed to be randomly distributed and stable within the material sample. Such assumptions bring us to the log-normal distribution for the flipping rates constant k_f:

$$P(\ln k_f) = \frac{\exp[-\ln^2 k_f / k_{fm}]}{(2\pi)^{1/2}\sigma_E} \tag{7}$$

Then to the sum the weighted spectra we write:

$$G(t) = \int_{-\infty}^{\infty} g(t, k_f) P(\ln k_f) d \ln k_f \tag{8}$$

where $g(t, k_f)$ is the individual simulated FID.

Passing to a discrete distribution we get:

$$G(t) = \sum_{i=1..N} g(t, k_f{}^i) W^i \tag{9}$$

Where the individual weights are computed as:

$$W^i = \frac{\int_{\ln k_f{}^i}^{\ln k_f{}^{i+1}} P(\ln k) d \ln k}{Norm} \tag{10}$$

The Norm is calculated as:

$$Norm = \sum_{i=1..N} W^i \tag{11}$$

Such modification to the original fitting routine allows us to take into account the rate exchange distribution for any motion(s). Within such an approach any rate constant will be characterized by 2 parameters: σ - the width of the distribution, and k_{fm} – the mean value of the rate constant, *i.e.,* the center of the distribution. The k_{fm} temperature behavior should characterize the mean Arrhenius parameters of the motion in the sample, *i.e.,* the activation barrier and collision factor. So, on a descriptive level, the sample at each temperature will be characterized by 3 population factors for: (a)

static on the ^{2}H NMR time-scale phenyl rings ($k_f < 10^3$ Hz << Q_0; $Q_0 = 176 \cdot 10^3$ Hz), (b) slowly mobile phenyls (10^3 Hz < k_f < 10^7 Hz) and (c) fast moving fragments ($k_f > 10^7$ Hz >> Q_0).

(1) Noguchi, H.; Hojo, K.; Suginome, M. *J. Am. Chem. Soc.* **2007**, *129*, 758.

(2) Vyas, V. S.; Banerjee, M.; Rathore, R.; *Tetrahedron Lett.* **2009**, *50*, 6159.

(3) Lin, X.; Telepeni, I.; Blake, A. J.; Dailly, A.; Brown, C. M.; Simmons, J. M.; Zoppi, M.; Walker, G. S.; Thomas, K. M.; Mays, T. J.; Hubberstey, P.; Champness, N. R.; Schröder, M. *J. Am. Chem. Soc.* **2009**, *131*, 2159.

(4) Rodríguez-Lojo, D.; Cobas, A.; Peña, D.; Pérez, D.; Guitián, E. *Org. Lett.* **2012**, *14*, 1363.

(5) Chichak, K.; Jacquemard, U.; Branda, N. R. *Eur. J. Inorg. Chem.* **2002**, *2002*, 357.

(6) Shustova, N. B.; Ong, T.-C.; Cozzolino, A. F.; Michaelis, V. K.; Griffin, R. G.; Dincă, M. *J. Am. Chem. Soc.* **2012**, *134*, 15061.

(7) Sheldrick, G. M. *Acta Crystallogr. A* **2008**, *64*, 112.

(8) Sheldrick, G. M. *Acta Crystallogr. Sect. C Struct. Chem.* **2015**, *71*, 3.

(9) Spek, A. L. *Acta Crystallogr. Sect. C Struct. Chem.* **2015**, *71*, 9.

(10) Rouquerol, J.; Llewellyn, P.; Rouquerol, F. In *Studies in Surface Science and Catalysis*; 2007; Vol. 160, pp 49–56.

(11) Rappe, A. K.; Casewit, C. J.; Colwell, K. S.; Goddard, W. A.; Skiff, W. M. *J. Am. Chem. Soc.* **1992**, *114*, 10024

(12) Gupta, A.; Chempath, S.; Sanborn, M. J.; Clark, L. A.; Snurr, R. Q. *Mol. Simul.* **2003**, *29*, 29.

(13) Jorgensen, W. L.; Laird, E. R.; Nguyen, T. B.; Tirado-Rives, J. *J. Comput. Chem.* **1993**, *14*, 206.

(14) Rappé, A. K.; Casewit, C. J.; Colwell, K. S.; Goddard Iii, W. A.; Skiff, W. M. *J. Am. Chem. Soc.* **1992**, *114*, 10024.

(15) Potoff, J. J.; Siepmann, J. I. *AIChE J.* **2001**, *47*, 1676.

(16) Walton, K. S.; Snurr, R. Q. *J. Am. Chem. Soc.* **2007**, *129*, 8552.

(17) O'koye, I. P.; Benham, M.; Thomas, K. M. *Langmuir* **1997**, *13*, 4054.

(18) Abragam, A. *The Principles of Nuclear Magnetism*; Oxford University Press, 1961.

(19) H. W. Spiess. Springer-Verlag, 1978; Vol. 15, p 55.

(20) Wittebort, R. J.; Szabo, A. *J. Chem. Phys.* **1978**, *69*, 1722.

(21) Wittebort, R. J.; Olejniczak, E. T.; Griffin, R. G. *J. Chem. Phys.* **1987**, *86*, 5411.

(22) Lipari, G.; Szabo, A. *Biophys. J.* **1980**, *30*, 489.

(23) Schwartz, L. J.; Meirovitch, E.; Ripmeester, J. A.; Freed, J. H. *J. Phys. Chem.* **1983**, *87*, 4453.